

# JWST Discovery of High-Velocity Mid-Infrared Ionized Outflows in Ultraluminous Infrared Galaxies F11119+3257 and F05189-2524

JEROME SEEBECK ,<sup>1</sup> KYLIE YUI DAN ,<sup>1</sup> SYLVAIN VEILLEUX ,<sup>1,2</sup> DAVID RUPKE ,<sup>3</sup> EDUARDO GONZALEZ-ALFONSO ,<sup>4</sup> ISMAEL GARCIA-BERNETE ,<sup>5</sup> WEIZHE LIU ,<sup>6</sup> DIETER LUTZ ,<sup>7</sup> MARCIO MELENDEZ ,<sup>8</sup> MIGUEL PEREIRA-SANTAELLA ,<sup>9</sup> ECKHARD STURM ,<sup>7</sup> AND FRANCESCO TOMBESI ,<sup>10,11,12</sup>

<sup>1</sup>Department of Astronomy, University of Maryland, College Park, MD 20742, USA

<sup>2</sup>Joint Space-Science Institute, Department of Astronomy, University of Maryland, College Park, MD 20742, USA

<sup>3</sup>Department of Physics, Rhodes College, Memphis, TN 38112, USA

<sup>4</sup>Universidad de Alcalá, Departamento de Física y Matemáticas, Campus Universitario, 28871 Alcalá de Henares, Madrid, Spain

<sup>5</sup>Centro de Astrobiología (CAB), CSIC-INTA, Camino Bajo del 497 Castillo s/n, E-28692 Villanueva de la Cañada, Madrid, Spain

<sup>6</sup>Department of Astronomy, Steward Observatory, University of Arizona, Tucson, AZ 85719, USA

<sup>7</sup>Max Planck Institute for Extraterrestrial Physics, Giessenbachstraße 1, 85748 Garching, Germany

<sup>8</sup>Space Telescope Science Institute, 3700 San Martin Drive, Baltimore, MD 21218, USA

<sup>9</sup>Instituto de Física Fundamental (IFF), CSIC, Serrano 123, E-28006 Madrid, Spain

<sup>10</sup>Physics Department, Tor Vergata University of Rome, Via della Ricerca Scientifica 1, 00133 Rome, Italy

<sup>11</sup>INFN – Rome Tor Vergata, Via della Ricerca Scientifica 1, 00133 Rome, Italy

<sup>12</sup>NASA Goddard Space Flight Center, Code 662, Greenbelt, MD 20771, USA

## ABSTRACT

Ultra-fast outflows (UFOs) are thought to be a driving mechanism of large-scale winds driven by active galactic nuclei, which cause significant galactic feedback through quenching star formation and regulating supermassive black hole growth. We present James Webb Space Telescope (*JWST*) Mid-Infrared Instrument Medium-Resolution Spectrometer observations of two nearby ultraluminous infrared galaxies (ULIRGs), F11119+3257 and F05189-2524, with nuclear X-ray detected UFOs and kiloparsec-scale outflow. These galaxies show remarkably similar mid-infrared continuum and emission line features, notably including a high-velocity  $v_{90} \sim 4000 \text{ km s}^{-1}$  outflow detected in highly ionized neon emission lines, e.g., [Ne VI]. In F05189-2524, we see a slightly slower biconical outflow extending up to  $\sim 2$  kpc in the same neon emission lines. Both sources show evidence of AGN-driven radiative feedback through a deficit of rotational molecular hydrogen lines in the nuclear region,  $<1$  kpc from the central quasar, but no clear evidence of any molecular gas entrained in the quasar-driven outflow. Energetic analysis shows that the warm ionized gas in both of these sources contributes minimally ( $\sim 0.1 – 5\%$ ) to the momentum outflow rate of these sources and leaves the conclusions of previous literature unchanged: the energetics of these sources are broadly consistent with a momentum-conserving outflow.

## 1. INTRODUCTION

UltraLuminous InfraRed Galaxies (ULIRGs) are a class of infrared (IR) bright ( $L_{\text{IR}} \geq 10^{12} L_{\odot}$ ) extragalactic sources, spanning a wide range of types from H II region-like to Seyfert 1 and 2, that were first discovered with the InfraRed Astronomical Satellite (IRAS) in 1984 (Houck et al. 1985). The bulk of their IR emission is due to energy re-radiated by warm dust excited by one or both of the two power sources: starburst and active galactic nuclei (AGN). Evidence showing a link between ULIRGs and galactic mergers has created a compelling theoretical picture: gas-rich galaxies merge, fueling gas into the galactic center and igniting dust-enshrouded

star formation and supermassive black hole accretion. These engines drive galactic winds which provide negative feedback through clearing dust and gas from the galaxy, limiting star formation and leaving an exposed optical quasar that ultimately becomes a red gas-poor elliptical galaxy (e.g., Sanders et al. 1988; Veilleux et al. 2009a,b; Hopkins et al. 2016; Hickox & Alexander 2018).

Evidence for these powerful winds is vital for our understanding of how inside-out negative feedback mechanisms work and has been detected in a majority of ULIRGs at a wide variety of physical scales and gas phases (e.g., molecular Veilleux et al. (2013), neutral atomic Rupke et al. (2017), warm ionized Rupke & Veilleux (2013), and hot ionized Veilleux et al. (2014);

Liu et al. (2019, 2022)). While many ULIRGs are dominated by starbursts (Veilleux et al. 2009a), high-velocity AGN-driven winds have been detected in a smaller subsample of sources (González-Alfonso et al. 2017; Rupke et al. 2017; Dan et al. 2025). This makes local AGN-dominated ULIRGs, which can be observed with high spatial resolution, an excellent test bench for the higher redshift universe where mergers and AGN are more prevalent and impactful (Hopkins et al. 2008; Zakamska et al. 2016), but direct observational evidence of feedback is limited (e.g. Veilleux et al. 2020). These luminous quasars are predicted to have significant effects on their host galaxies, including, but not limited to, galaxy morphology (e.g., Dubois et al. 2016; Choi et al. 2018), the interstellar medium (e.g., Hopkins et al. 2016; Davé et al. 2019), the circumgalactic medium (e.g., Tumlinson et al. 2017), supermassive black hole growth (e.g., Volonteri et al. 2016; Hopkins et al. 2016), and star formation quenching (Zubovas & King 2012; Pontzen et al. 2017).

Some models predict that galactic-scale AGN-driven winds are powered by sub-parsec-scale ultra-fast outflows (UFOs) (Zubovas & King 2012; Wagner et al. 2013; King & Pounds 2015; Gaspari et al. 2020; Costa et al. 2020; Laha et al. 2021). These UFOs are initially accelerated through radiatively or magnetically driven mechanisms based on the accretion rate of the SMBH (e.g., Gallo et al. 2023) and have been observed in numerous sources (Tombesi et al. 2010, 2014; Matzeu et al. 2023; Xrism Collaboration et al. 2025). Energy from the UFO is then deposited into the nuclear ISM, shocking the nearby gas, and creating an expanding hot bubble. If this bubble is unable to cool efficiently, then it will continue to expand adiabatically in an energy-conserving phase and produce a high ratio of the outer momentum outflow to the inner momentum outflow, powered by the UFO ( $\dot{P}_{\text{outer}}/\dot{P}_{\text{inner}} > 1$ ). If the energy from the hot wind is radiated away, then the resulting outflow is expected to be momentum-conserving ( $\dot{P}_{\text{outer}}/\dot{P}_{\text{inner}} \lesssim 1$ ) and driven largely by ram pressure. There is no clear consensus on a dominant outflow coupling mechanism, and evidence for both energy-conserving and momentum-conserving outflows has been reported (e.g., Veilleux et al. 2005; Tombesi et al. 2015; Smith et al. 2019; Veilleux et al. 2020; Marasco et al. 2020; Laha et al. 2021; Lanzuisi et al. 2024).

In this paper, we analyze the mid-infrared emission of two AGN-dominated, late-stage merger ULIRGs with X-ray detected UFOs, F11119+3257 and F05189-2524, in order to search for and parameterize outflow dynamics and other evidence of AGN feedback. In Section 2, we discuss the observations and reduction of the *JWST*

data. We discuss our analysis methods, including the use of the integral-field unit spectroscopy (IFS) analysis software package `q3dfit`, in Section 3. In Section 4 we present the results of our analysis of both extracted spectra and IFS kinematic maps. In Section 5, we discuss the evidence and energetics of the high-velocity outflow of both sources. We summarize our conclusions in Section 6

For this paper, we adopt the flat  $\Lambda$ CDM cosmology:  $H_0 = 70 \text{ km s}^{-1} \text{ Mpc}^{-1}$ ,  $\Omega_m = 0.3$  and  $\Omega_\Lambda = 0.7$ . For F11119+3257, we use a redshift of  $z = 0.19 \pm 0.01$ , derived by Pan et al. (2019). This gives a luminosity distance  $D_L = 925.6 \text{ Mpc}$  and a physical scale of  $1'' = 3.169 \text{ kpc}$ . For F05189-2524, we use a redshift of  $z = 0.042731$ , derived by Lamperti et al. (2022). This gives a luminosity distance  $D_L = 172.4 \text{ Mpc}$  and a physical scale of  $1'' = 0.848 \text{ kpc}$ . All emission lines are identified by their wavelengths in vacuum (e.g., [O III]  $\lambda 5008 \text{ \AA}$ ).

### 1.1. *F11119+3257*

IRAS F11119+3257 is a relatively nearby ( $z = 0.19$ ) Seyfert 1 late-stage merger ULIRG and has a  $L_{\text{bol}} \sim 10^{46.3} \text{ erg s}^{-1}$ , 71% of which is attributed to AGN emission (Veilleux et al. 2009a). F11119+3257 was the first source to have confirmed observations of both galactic-scale and sub-parsec relativistic outflows (Tombesi et al. 2015). This was a spectacular link between central AGN-powered winds and galactic-scale feedback. The nuclear wind was detected through Suzaku Fe K absorption observations (later confirmed with NuSTAR Tombesi et al. 2017), which showed a  $v_{\text{out}} \sim 0.3c$  outflow with a momentum outflow rate similar to that input by the central black hole. Recent XMM-Newton and NuSTAR observations (Lanzuisi et al. 2024) have confirmed the UFO and estimated a slightly higher momentum outflow rate,  $\sim 6L_{\text{bol}}/c$ . Unresolved cold molecular outflows, traced by OH and modeled to a distance of 300 pc (Tombesi et al. 2015), imply that the energy has been conserved from this UFO to the galactic-scale outflow. Updated CO (1-0) observations from Veilleux et al. (2017) show an extended outflow not inconsistent with a momentum-conserving flow. Spatially resolved outflow has not been detected for any gas phase in this source.

### 1.2. *F05189-2524*

IRAS F05189-2524 is a relatively nearby ( $z = 0.042731$ ) Seyfert 2 late-stage merger ULIRG with a broad line region observed in the near-infrared (Veilleux et al. 1999). It is an extremely X-ray bright source with a Fe K absorption feature blueshifted from  $E = 6.966$  to  $7.8 \text{ keV}$ , implying an UFO with  $v_{\text{out}} = 0.11c$  (Smith et al. 2019). This UFO was recently confirmed

by XRISM with the detection of three separate Fe K absorption features in the 7.8 keV region, ranging from 0.76c – 0.143c (Noda et al. 2025). F05189-2524 has a  $L_{\text{bol}} \sim 10^{45.8}$  erg s $^{-1}$ , 69% of which is attributed to AGN emission (Veilleux et al. 2009a). Previous observations have shown spatially resolved and unresolved high-velocity outflows in many phases of gas. Cold molecular outflows, traced by OH and CO (González-Alfonso et al. 2017; Fluetsch et al. 2019; Lutz et al. 2020; Lamperti et al. 2022), show a momentum outflow rate of  $\sim 3 L_{\text{bol}}/c$ . IFS observations of resolved outflows,  $R_{\text{out}} \leq 3$  kpc, with median velocities  $\sim 500$  km s $^{-1}$  in neutral gas, traced by Na I D 5890, 5896 Å, and warm ionized gas, traced by [N II] 6585 Å, show momentum boosts of  $\sim 3 L_{\text{bol}}/c$  and  $\sim 0.04 L_{\text{bol}}/c$ , respectively (Rupke et al. 2017).

## 2. OBSERVATIONS AND DATA REDUCTION

Both F11119+3257<sup>1</sup> and F05189-2524<sup>2</sup> were observed using the Medium-Resolution Spectrometer (MRS) mode of the Mid-Infrared Instrument (Wright et al. 2023; Argyriou et al. 2023, MIRI). All of the grating settings, Short, Medium, and Long, were used to achieve the full wavelength range of MIRI (4.9 to 27.9  $\mu\text{m}$ ). The spectral resolution of MIRI ranges from 8 Å in channel 1 to 60 Å in channel 4, corresponding to 30 – 85 km s $^{-1}$  across the entire MIRI wavelength range. A 4-point extended dither pattern was used to help remove background contamination and reduce undersampling. F11119+3257 was observed on May 23, 2024 (PID 3869, PI Veilleux) and F05189-2524 was observed on March 4, 2024 (PID 3368, PI Armus).

We reduced these data with *JWST* v1.15.1 (Bushouse et al. 2022; Bushouse et al. 2024) and v12.0.2 of the Calibration Reference Data System (CRDS). The reduction is done with the MIRI pipeline sample notebook publicly available on the Space Telescope github ([MRS\\_FlightNB1.ipynb](#)) with the 2D, pixel-by-pixel, background subtraction step turned on and the rest of the notebook in its default state. This step noticeably improves the overall noise in fully reduced cubes.

We can see the results from the *JWST* pipeline applied to F05189-2524 in Figure 1, which displays spaxels from sub-bands in each MIRI channel as the gray spectra. Two types of fringing remain in these reduced cubes. The first can be seen in panels (c) and (d) of Figure 1, showing large fringes at the edge of the MIRI

bands but minimal fringing near the center. This is caused by spatial undersampling, which is an expected side effect of maximizing the field of view (FOV) and spectral resolution of *JWST* (Law et al. 2023). The recommended solution for this issue is to extract spectra with a width similar to that of the PSF.

The second type of fringing is seen across all 4 channels and increases with higher frequencies. To mitigate this, we take a two-step approach to correct each MRS sub-band individually. First, we smooth the cube with a running circular average using a radius of 1.5 pixels, seen as the purple spectra in Figure 1. This smoothing eliminates the fringes caused by spatial undersampling and increases the S/N ratio of the higher frequency fringes. Second, we apply the *JWST* pipeline function `fit_residual_fringes_1d` spaxel-by-spaxel to the reduced cubes; the final sample spectra can be seen as the red spectra in Figure 1. We find that the efficacy of this function is significantly improved by the previous smoothing step. In our final re-reduced cube, we find that both fringing types are eliminated or significantly reduced in a majority of spaxels, allowing for much more detailed analysis of line kinematics.

For spatial comparisons of spectrally distant emission lines, we apply two more reduction steps. First, we spatially smooth a set of the final reduced cubes for each sub-band individually, unifying the effective PSF size to the observed wavelength of the H<sub>2</sub> S(1) 17.03  $\mu\text{m}$  line. This is the emission line with the longest wavelength that we analyze with spatially resolved data and corresponds to a final PSF FWHM of 1.46'' for F11119+3257 and 0.99'' for F05189-2524. We estimate the wavelength-dependent PSF FWHM of MIRI MRS from the value observed in 3D drizzled cubes (Figure 12 of Argyriou et al. 2023). Then, at every wavelength, we calculate the quadrature difference ( $\sigma_{\text{convolve}} = \sqrt{\sigma_{17.03}^2 - \sigma_{\lambda}^2}$ ) to the PSF FWHM of the H<sub>2</sub> S(1) 17.03  $\mu\text{m}$  line and convolve the slice with a 2D Gaussian with  $\sigma = \sigma_{\text{convolve}}$ . Second, we coarsely stitch the cubes together to remove the effects of any flux discontinuities in a similar method to that described in Ceci et al. (2025). To do this, we first rescale the flux down to the lowest spatial resolution channel using the flux-conserving method in the package `reproject` (Robitaille et al. 2024). For both sources, this is again limited by the longest wavelength observed line H<sub>2</sub> S(1) 17.03  $\mu\text{m}$ . For F11119+3257, this limits the spatial resolution to that of Channel 3, 0.2''/pixel, and for F05189-2524, the resolution is limited to that of Channel 4, 0.35''/pixel. Then, we stitch the cubes together by scaling the emission of the bluer cube to match the flux of the redder cube in each spaxel, starting with the reddest channel used in the analysis of each source.

<sup>1</sup> The *JWST* MIRI/MRS data used for F11119+3257 in this paper can be found in MAST: [10.17909/1bgd-mf94](#).

<sup>2</sup> The *JWST* MIRI/MRS data used for F11119+3257 in this paper can be found in MAST: [10.17909/5zxm-mq78](#).

This results in a continuous spectrum in each spaxel of the data cube across the entire MIRI range. We only use these cubes when direct spaxel-to-spaxel comparisons need to be made of emission lines not in the same sub-band and will defer to the higher spatial resolution of the non-unified cubes otherwise. We will refer to these cubes as the “unified” cubes.

For the 1D spectral analysis, we follow a similar method to [Seebeck et al. \(2024\)](#), extracting a nuclear spectrum for both sources out of data cubes directly from the pipeline using an aperture with a  $\text{FWHM}(\lambda) = 0.7''$  for  $\lambda < 8 \mu\text{m}$  and  $\text{FWHM}(\lambda) = 0.7'' \times \lambda[\mu\text{m}]/8 \mu\text{m}$  for  $\lambda \geq 8 \mu\text{m}$ . Data from each channel are first defringed using the `fit_residual_fringes_1d` function and then concatenated to form a longer spectrum. For overlapping regions, we take the average of both sub-bands which causes no spectral jumps as seen in the final extracted spectra in Figure 2. We have rebinned the spectrum on the grid with  $\Delta\lambda = 8 \text{ \AA}$ , the spectral element width of Channel 1. The rebinning causes no significant change ( $\leq 2\%$ ) in the fluxes of longer wavelength lines but improves the flux measurements of shorter wavelength lines by up to 20% from measurements using the coarser spectral width of Channel 4.

### 3. DATA ANALYSIS

#### 3.1. Nuclear Spectrum Fitting

To fit the nuclear spectrum of both sources, we use two methods. First, we use the `q3dfit` adaptation of `questfit` ([Schweitzer et al. 2008; Rupke et al. 2021](#)) to fit larger continuum features. While this method is effective in fitting broad continuum features, it is less reliable over narrow wavelength regions, causing the line fits to be less accurate. To make line flux measurements, we use the `q3dfit` method `polyfit` to more effectively subtract the continuum from nearby emission lines.

`questfit` was built to fit mid-infrared (MIR) spectra of galaxies from the *Spitzer* Quasar and ULIRG Evolution Study (QUEST; [Veilleux et al. 2009a](#)). It uses polycyclic aromatic hydrocarbon (PAH) templates ([Smith et al. 2007](#)), silicate templates ([Schweitzer et al. 2008; Groves et al. 2006](#)), extinction and absorption models, and blackbodies of various temperatures. In using `questfit` for the fitting of our extracted nuclear spectra, we follow the same methods as [Seebeck et al. \(2024\)](#), which follows a similar procedure to that described in [Veilleux et al. \(2009a\)](#).

To fit PAH features, we subtract the non-PAH emission of the `questfit` model from the extracted spectrum and directly fit the PAH residuals. We extract fluxes from the PAH 6.2, 7.7, 11.3, and 12.7  $\mu\text{m}$  features by simultaneously fitting their main features with

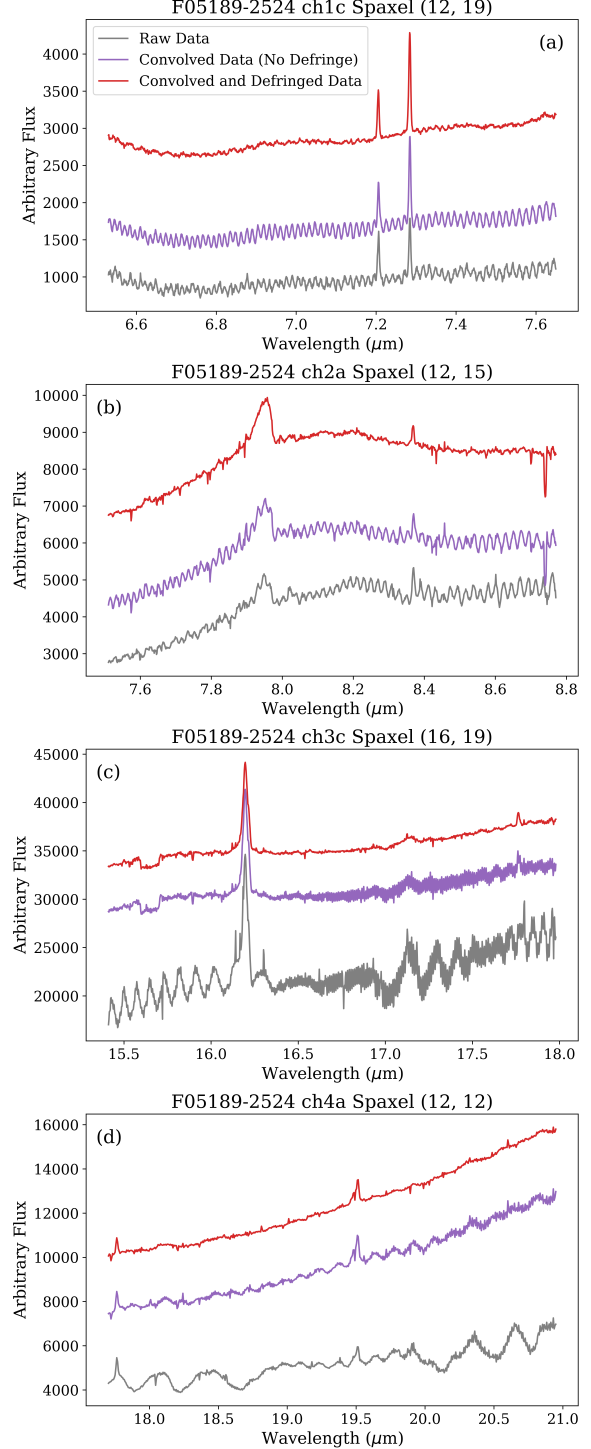


**Figure 1.** Spectra extracted from 4 sample spaxels, one for each MIRI channel, showing the post *JWST* pipeline defringing process for the source F05189-2524. Each subplot shows the raw data directly from the *JWST* pipeline (gray), the data smoothed with a running circular average using a radius of 1.5 spaxels (purple), and the final resulting spectra which has been smoothed and defringed using the *JWST* pipeline function `fit_residual_fringes_1d` (red).

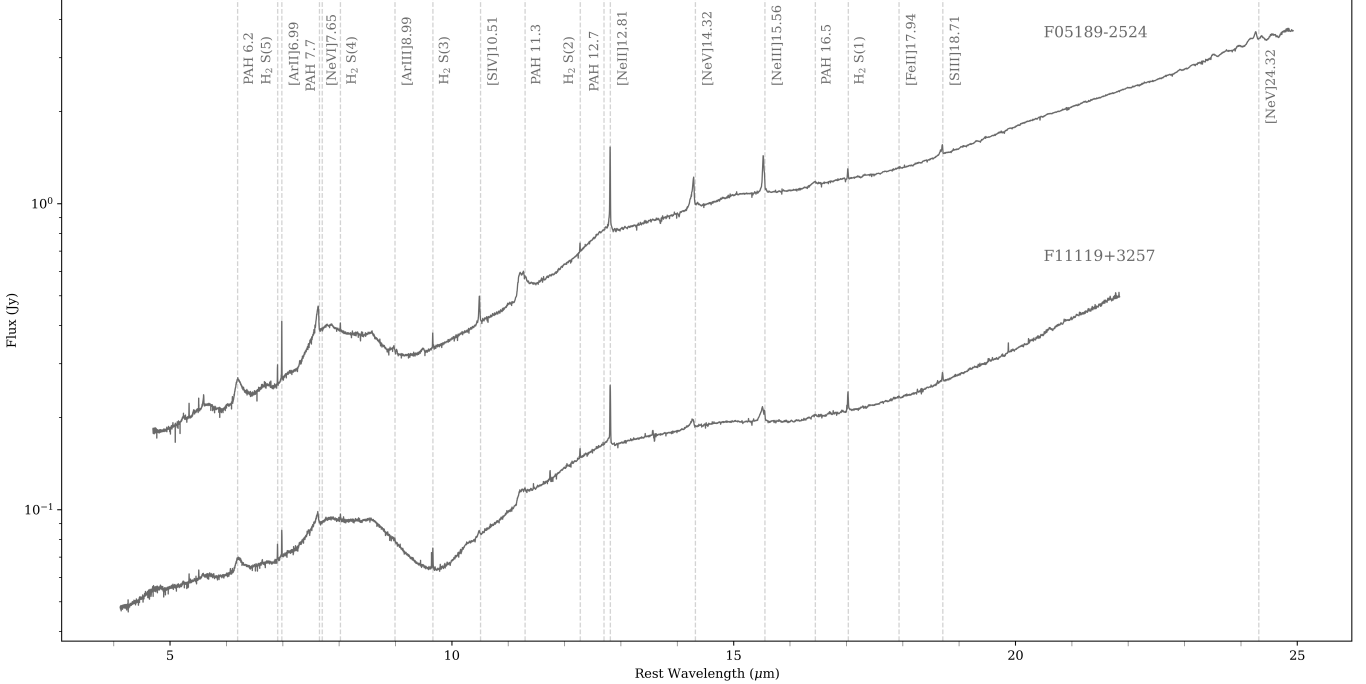


**Figure 2.** 1D nuclear spectra of F05189-2524 (top) and F11119+3257 (bottom) extracted from the *JWST* pipeline data cube and corrected for residual fringes. Common MIR spectral features are marked with vertical dashed lines at their rest wavelengths.

a sum of Lorentzian profiles superimposed on a continuum approximated by a second-order polynomial. This follows the methods described in [Seebeck et al. \(2024\)](#) and [Schweitzer et al. \(2006\)](#) and should give similar values to those derived in [Rigopoulou et al. \(2021\)](#).

### 3.2. Integral Field Spectroscopy Fitting

We use the software package `q3dfit` for the majority of our analysis ([Rupke et al. 2023a](#)). This package is based on the IDL software `IFSFIT` ([Rupke 2014](#); [Rupke et al. 2017](#)), designed to remove the PSF caused by the central compact quasar emission, allowing us to see the much fainter emission from the host galaxy without contamination from the bright PSF. This tool is ideally suited for the analysis of IFS AGN data, as without removing a dominant PSF, the compact nuclear region overwhelms emission from extended regions of the galaxy. More details on the `q3dfit` software and its use in the analysis of *JWST* IFS data can be found in [Veilleux et al. \(2023\)](#); [Rupke et al. \(2023b\)](#); [Vayner et al. \(2023\)](#).

In our fits, we use a spectrum extracted from the brightest spaxel in the data as a quasar template. In an initial fit, the template, in combination with emission lines and an exponential starlight model, is fit to the data. The template is scaled up or down with a series of exponentials to match the continuum level of different spaxels and remove data that resembles the nuclear spectrum. These initial fits may then be used as

initial guesses in a second stage of fitting where more detailed models, such as stellar population synthesis, can be used to lower the residuals. The process then loops, refitting emission lines and the total sum continuum until certain residual levels in the relative error of the approximate solution and desired sum of squares are met. Line profiles are fit with a specified number of Gaussian components to the spectrum with starlight and nuclear emission removed. `q3dfit` also imposes a significance cut on each component of each line every iteration. If the fit is not significant enough, it will be removed and fit with fewer components or not fit at all. This entire process is done for every spaxel in the data and can be accelerated with multicore processing. Due to a lack of obvious stellar absorption features in the data, the use of exponential starlight models was only used sparingly in certain spaxels to improve the continuum fit.

To reduce computational times and improve fit quality, we run all of our `q3dfit` analysis in the sub-band where each line is observed. `q3dfit` relies on strong initial guesses for the central velocity and width of Gaussian line components. When two non kinematically tied lines with very distinct kinematic components are present in the same sub-band, even the perfect initial guess can cause false-positive or negative results in the fits. To mitigate this problem, we occasionally fit the sub-band separately for the different lines.

## 4. RESULTS

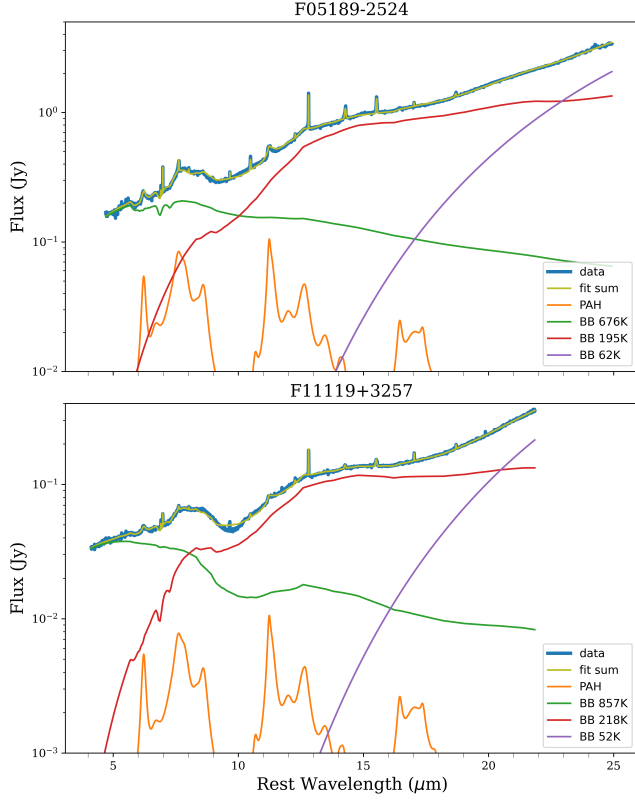


**Figure 3.** Fit of 1D extracted spectrum (blue) with `questfit` the continuum fitting package within `q3dfit` for F05189-2524 (top) and F11119+3257 (bottom). Each spectrum is fit with three black bodies with different temperatures, cool (purple), warm (red), and hot (green), and a PAH template (orange). The total sum fit is the yellow curve.

#### 4.1. Nuclear Emission

Our fitting methods well approximate the continuum of both sources with slight fitting residuals near the  $\tau_{9.7}$  silicate absorption and some emission lines. These fits are shown in Figure 3. Our PAH measurements are listed in Table 1. Due to minor continuum fitting issues in F11119+3257, we are only able to set upper limits on the  $12.7\text{ }\mu\text{m}$  PAH feature based on the fit PAH template instead of directly fitting the residuals as in the other features. We find our  $6.2$  and  $7.7\text{ }\mu\text{m}$  feature measurements consistent, within error bars and expected instrumental aperture differences, with results from *Spitzer* data in Veilleux et al. (2009a). There are no previous measurements of the  $11.3$  and  $12.7\text{ }\mu\text{m}$  PAH features. Our results show that the equivalent widths ( $\text{EW} = F(\text{PAH})/F_{\lambda,\text{cont}}(\lambda_{\text{PAH}})$ ) of PAH features are stronger in F05189-2524 than in F11119+3257, but the overall PAH luminosities are larger in F11119+3257 than in F05189-2524.

We fit 19 emission lines (11 ionized and 8 molecular) in F11119+3257 and 25 emission lines (17 ionized and 8 molecular) in F05189-2524. For both sources, emission lines are fit with one component except [Ne III], [Ne V], and [Ne VI] (3 components) and [Mg V], [Ar III], and [Ne II] (2 components). The  $v_{50}$  and  $w_{80}$  of the ionized gas fit is shown in Figure 4 plotted against the ionization potential (IP) and critical density (gathered from PyNeb, Luridiana et al. 2015) of the gas.  $v_{50}$  is the 50-percentile or median velocity: the velocity where 50% of the line flux is accumulated as calculated from the red side of the profile.  $w_{80}$  is the 80-percentile velocity width: the velocity width of the line containing 80% of line flux, centered on  $v_{50}$ . See Veilleux (1991a,b,c); Zakamska & Greene (2014) for a more detailed description and validation of these measurements. The fluxes,  $v_{50}$ , and  $w_{80}$  from all line fits, for both sources are shown in Table 2. Both sources show a significant increase in both the  $|v_{50}|$  and  $w_{80}$  with increases in IP but no significant trend for the critical density. F11119+3257 shows a steeper correlation between outflow velocities and IP than F05189-2524. The high velocities, IPs, and positive correlation between the two are possibly indicative of a decelerating AGN-driven outflow, first proposed in the MIR by Spoon & Holt (2009). Another possible explanation for this trend is that the outflow is spatially stratified with larger velocities and IP emission closer to the outflow axis and slower velocities towards the edges, as supported by simulations (e.g. Schneider & Mao 2024, and references therein).

The positive correlation between  $|v_{50}|$  and IP is best illustrated by the sequence of strong MIR neon emission lines ([Ne II]  $12.81\text{ }\mu\text{m}$ , [Ne III]  $15.56\text{ }\mu\text{m}$ , [Ne V]  $14.32\text{ }\mu\text{m}$ , and [Ne VI]  $7.65\text{ }\mu\text{m}$ ). We show the kinematic fits to four neon emission lines for both sources in Figure 5. The emission from both sources is remarkably similar. The lowest IP line [Ne II] primarily shows narrow line emission at near systemic velocities with a possible weak outflow  $v_{50} \sim -1000\text{ km s}^{-1}$  potentially contaminated by emission from a PAH feature at  $12.7\text{ }\mu\text{m}$ . The central peak of the remaining three lines is increasingly blueshifted with respect to the IP of the lines (up to  $v_{50} \sim -1500\text{ km s}^{-1}$  in [Ne VI]), and the broad, blueshifted wing increases in strength and blueshift along the same sequence (up to  $v_{90} \sim -4000\text{ km s}^{-1}$  in [Ne VI]). Evidence of systemic emission is still seen in [Ne III] but not in [Ne V] or [Ne VI]. These same trends are seen in other elemental series in both sources (e.g., argon, sulfur, and sodium) see Table 2 for more details.

**Table 1.** PAH Measurements

PAH Feature	Source	6.2 $\mu\text{m}$	7.7 $\mu\text{m}$	11.3 $\mu\text{m}$	12.7 $\mu\text{m}$
$\lambda$ range ( $\mu\text{m}$ )		5.9 – 6.5	6.9 – 9.2	10.8 – 11.7	12.5 – 12.8
EW <sup>a</sup>	F11119+3257	2.6 (0.5)	7.3 (4.0)	1.4 (0.8)	$\leq 2.1^*$
	F05189-2524	4.6 (1.4)	25.8 (7.8)	3.4 (0.3)	2.4 (1.1)
Flux <sup>b</sup>	F11119+3257	0.9 (0.1)	2.2 (1.1)	0.3 (0.1)	$\leq 0.4^*$
	F05189-2524	9.0 (1.0)	36.2 (11.9)	3.6 (0.3)	3.2 (1.4)
Luminosity <sup>c</sup>	F11119+3257	2.3 (0.1)	5.7 (3.0)	0.7 (0.2)	$\leq 1.2^*$
	F05189-2524	1.0 (0.2)	4.1 (1.2)	0.4 (0.1)	0.4 (0.2)

<sup>a</sup>In units of  $10^{-2} \mu\text{m}$

<sup>b</sup>In units of  $10^{-13} \text{ erg s}^{-1} \text{ cm}^{-2}$

<sup>c</sup>In units of  $10^9 L_\odot$

$*$ Upper limits derived from PAH template fits

NOTE—Errors for our PAH fits are listed (in parentheses) and are taken from the standard error of the least squares fit to the data.

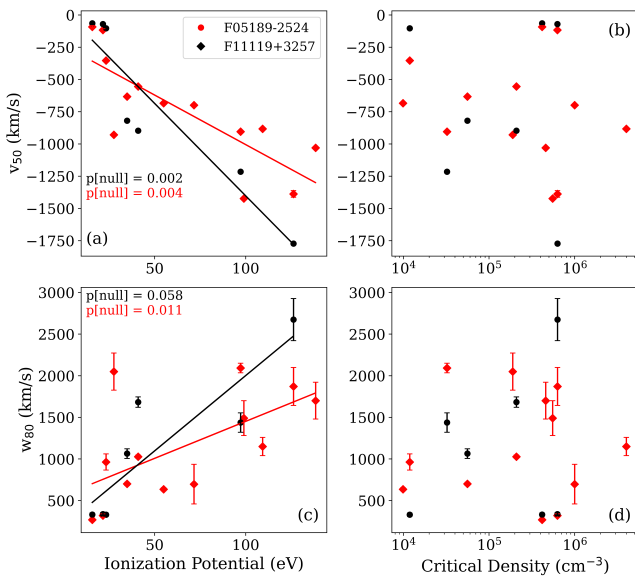


**Figure 4.** Left column: plot of  $v_{50}$  (top left) and  $w_{80}$  (bottom left) vs ionization potential. Right column: plot of  $v_{50}$  (top right) and  $w_{80}$  (bottom right) vs critical density. Data points represent all ionized gas emission lines fit in F11119+3257 (black) and F05189-2524 (red). The data for all plots are fit with a linear regression and any fits with a  $p[\text{null}] < 0.1$  are displayed on the plot and the  $p[\text{null}]$  for significant fits is listed with the corresponding color for the correct source

A few small differences are present between the emission of both sources. In all lines, the emission from F11119+3257 is generally slightly more blueshifted and broader, consistent with Figure 4. In [NeV] emission

from F05189-2524, a distinct redshifted component is visible centered near  $750 \text{ km s}^{-1}$ ; no such component is present in any of the F11119+3257 lines. The continuum noise in F05189-2524 is weaker than in F11119+3257, causing individual line components to be slightly more distinct in F05189-2524.

The molecular gas fits ( $\text{H}_2 0 - 0 \text{ S}(1) - \text{S}(8)$ ) for both sources are kinematically very similar. They both show no clear signs of outflow and exhibit a slight blueshift, with average median velocities (for all lines) of  $v_{50}^{\text{F05189}} \sim -110 \text{ km s}^{-1}$  and  $v_{50}^{\text{F11119}} \sim -60 \text{ km s}^{-1}$  and are narrower than the ionized lines with average velocity widths of  $w_{80}^{\text{F05189}} \sim 250 \text{ km s}^{-1}$  and  $w_{80}^{\text{F11119}} \sim 320 \text{ km s}^{-1}$ .

## 4.2. Extranuclear Emission

### 4.2.1. Low Velocity

Both sources show evidence of extended emission of rotational  $\text{H}_2$  and low IP warm ionized gas lines at low, near-systemic, velocities. We run a `q3dfit` analysis of the rotational  $\text{H}_2$  lines from S(1) to S(7) for both sources on the non-unified cubes. In F05189-2524, we additionally detect and fit the S(8) transition, but any higher transitions are outside of the MRS observed wavelengths. The higher redshift of F11119+3257 brings the S(9), S(10), and S(11) transitions into view, but they are too weak relative to the continuum noise to detect. For both sources, we fit the  $[\text{Ar II}] 6.99 \mu\text{m}$  and  $[\text{Ne II}] 12.81 \mu\text{m}$  ionized lines due to their strength, evidence for low-velocity extended emission, and because they lie in the same sub-bands as the S(5) and S(2)  $\text{H}_2$  lines, making them good references for warm ionized gas emission. For

**Table 2.** Nuclear Results

Feature ID	$\lambda_{rest}$	IP	F05189-2524				F11119+3257		
			$\mu\text{m}$	eV	Flux	$v_{50}$	$w_{80}$	Flux	$v_{50}$
					$10^{-14} \text{ erg s}^{-1} \text{ cm}^{-2}$	$\text{km s}^{-1}$	$\text{km s}^{-1}$	$10^{-14} \text{ erg s}^{-1} \text{ cm}^{-2}$	$\text{km s}^{-1}$
$\text{H}_2 0 - 0 \text{ S}(8)$	5.05	—	0.3 (0.2)	—	-130 (10)	310 (103)	0.1 (0.1)	-90 (10)	270 (54)
$[\text{Fe II}]$	5.34	7.9	0.9 (0.1)	—	-100 (10)	260 (20)	0.2 (0.1)	-70 (10)	320 (23)
$\text{H}_2 0 - 0 \text{ S}(7)$	5.51	—	0.8 (0.1)	—	-120 (10)	230 (20)	0.2 (0.1)	-40 (10)	300 (21)
$[\text{Mg V}]$	5.61	109.3	2.6 (0.7)	—	-870 (10)	1040 (145)	0.2 (0.1)	-1430 (10)	1340 (218)
$\text{H}_2 0 - 0 \text{ S}(6)$	6.11	—	0.4 (0.1)	—	-100 (10)	260 (20)	0.1 (0.1)	-20 (10)	560 (83)
$[\text{N II}]$	6.64	14.5	0.5 (0.2)	—	-10 (10)	730 (144)	0.1 (0.1)	0 (10)	620 (70)
$\text{H}_2 0 - 0 \text{ S}(5)$	6.91	—	1.3 (0.7)	—	-90 (10)	240 (66)	0.3 (0.1)	-70 (10)	270 (20)
$[\text{Ar II}]$	6.99	15.8	5.1 (0.2)	—	-90 (10)	270 (20)	0.6 (0.1)	-60 (10)	330 (20)
$[\text{Na III}]$	7.32	47.3	0.8 (0.2)	—	-600 (10)	680 (75)	0.1 (0.1)	-740 (10)	1100 (257)
$[\text{Ne VI}]$	7.65	126.2	13.5 (3.0)	—	-1310 (17)	1670 (188)	1.7 (0.3)	-1770 (10)	2670 (253)
$\text{H}_2 0 - 0 \text{ S}(4)$	8.03	—	0.7 (0.3)	—	-120 (10)	270 (51)	0.2 (0.1)	-70 (10)	560 (56)
$[\text{Na VI}]$	8.61	138.4	0.6 (0.2)	—	-1000 (10)	850 (110)	—	—	—
$[\text{Ar III}]$	8.99	27.6	3.2 (0.5)	—	-1020 (10)	2210 (183)	—	—	—
$[\text{Na IV}]$	9.04	71.6	0.3 (0.3)	—	-680 (10)	540 (217)	—	—	—
$[\text{Fe VII}]$	9.53	99.0	1.2 (0.3)	—	-1450 (10)	1520 (221)	—	—	—
$\text{H}_2 0 - 0 \text{ S}(3)$	9.66	—	1.0 (0.1)	—	-100 (10)	250 (20)	0.3 (0.1)	-40 (10)	310 (20)
$[\text{S IV}]$	10.51	34.9	5.0 (0.2)	—	-630 (10)	680 (20)	0.2 (0.1)	-820 (10)	1060 (58)
$\text{H}_2 0 - 0 \text{ S}(2)$	12.28	—	0.8 (0.1)	—	-100 (10)	220 (20)	0.2 (0.1)	-80 (10)	280 (20)
$[\text{Ne II}]$	12.81	21.6	18.8 (0.6)	—	-130 (10)	590 (20)	2.5 (0.1)	-110 (10)	950 (26)
$[\text{Ne V}]$	14.32	97.2	17.1 (0.9)	—	-920 (10)	1520 (41)	0.7 (0.1)	-1220 (10)	1440 (117)
$[\text{Ne III}]$	15.56	41.0	16.3 (0.6)	—	-560 (10)	980 (20)	1.6 (0.1)	-900 (10)	1680 (63)
$\text{H}_2 0 - 0 \text{ S}(1)$	17.03	—	1.3 (0.1)	—	-140 (10)	280 (20)	0.5 (0.1)	-100 (10)	340 (20)
$[\text{Fe II}]$	17.94	—	0.3 (0.2)	—	-70 (10)	860 (189)	—	—	—
$[\text{S III}]$	18.71	23.3	3.3 (0.7)	—	-340 (10)	900 (91)	0.2 (0.0)	-100 (10)	330 (20)
$[\text{O III}]$	25.89	54.9	12.2 (0.8)	—	-680 (10)	580 (20)	—	—	—

NOTE—Uncertainties on these fits, listed in parentheses next to the values, are calculated by `q3dfit` using the residuals from the line fit for the flux and from the fit covariance matrix for the sigma. A minimum uncertainty of  $10 \text{ km s}^{-1}$  for  $v_{50}$  and  $20 \text{ km s}^{-1}$  for  $w_{80}$  has been imposed based on instrumental limits. We use these uncertainties for all lines fit with `q3dfit`.

these fits, we kinematically tie the velocity and velocity dispersion of the ionized gas emission to the molecular emission in order to reduce noise in the ionized gas fits as the lines trace kinematically similar emission but the molecular lines are stronger in the extended emission. We run the same `q3dfit` analysis on the unified cubes, which give consistent results with those described below. The results of the fitting of two of the strongest and best resolved molecular lines, S(3) and S(5), are shown in Figure 6 for both sources. We show maps of the quasar-subtracted flux,  $v_{50}$ , and  $w_{80}$ .

For F11119+3257, the  $v_{50}$  velocity field for both molecular lines shows a low-velocity gradient,  $v_{50,red} - v_{50,blue} \sim 200 \text{ km s}^{-1}$ , from northwest (blueshifted) to

the southeast (redshifted). This is likely attributed to disk rotation, confirmed by ALMA CO (1-0) measurements (Veilleux et al. 2017). The extent of this gradient and the excess emission are greater in S(3) than S(5), extending to  $\sim 5$  kpc from the nucleus at its greatest extent. Both lines show a slight decrement of flux in the inner kpc, which we attribute to an artifact of the PSF subtraction. Following methods used in Liu et al. (2020) derived from Veilleux et al. (2020), we used velocity measurements from the best spatially and spectrally resolved line S(5) to measure a conservative lower limit on the circular and escape velocities of F11119+3257. We measure a  $v_{\text{circ}} = \sqrt{v_{\text{H}_2}^2 + 2\sigma_{\text{H}_2}^2} = 130 \text{ km s}^{-1}$  and a  $v_{\text{esc}} \simeq 3v_{\text{circ}} = 390 \text{ km s}^{-1}$  by taking observed maxi-

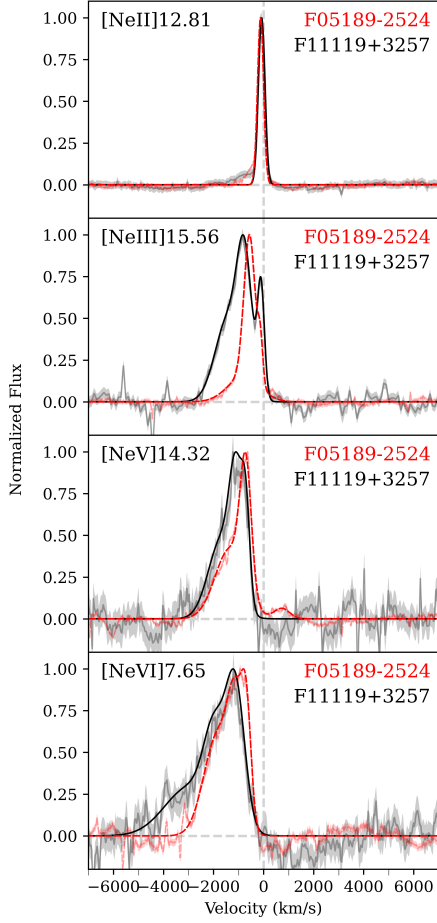


**Figure 5.** Fits to the MIR neon emission lines extracted from the nuclear, unresolved emission of F11119+3257 (red dashed) and F05189-2524 (black). The data are shown in light red dashed for F11119+3257 and gray for F05189-2524 with the  $1-\sigma$  error range filled in with the corresponding color for each source. The kinematics of each line are fit with up to three independent Gaussians. There is weak PAH emission at  $12.7\ \mu\text{m}$  just to the blue side of [Ne II], which is difficult to decouple from [Ne II] emission.

mum values in the inner rotating disk. These methods give a conservative lower limit through assumptions of a density profile of a truncated single isothermal sphere, no inclination, and a constant density between the quiescent and outflowing gas.

For F05189-2524, the larger spatial scale causes the excess emission to push the boundaries of the MRS FOV, extending up to  $\sim 3$  kpc in S(1), the line in the sub-band with the largest FOV. S(5) shows clear evidence of a low-velocity gradient,  $v_{50,\text{red}} - v_{50,\text{blue}} \sim 100\ \text{km s}^{-1}$ , from the west (blueshifted) to the east (redshifted) in the inner kpc of the galaxy. This gradient is marginally seen in S(3), but the lower spatial resolution makes it difficult to confirm, as inner spaxels are more confounded

by PSF removal. This gradient is confirmed by other high spatial resolution molecular lines (Lutz et al. 2020; Lamperti et al. 2022) and is consistent with stellar velocities (Rupke et al. 2017). A spectrally broad, redshifted clump is seen  $\sim 1$  kpc to the northwest in both lines with a  $v_{50} \sim 100\ \text{km s}^{-1}$  and a  $w_{80} \sim 500\ \text{km s}^{-1}$ . The rest of the field shows patchy blue and redshifted emission with  $|v_{50}| \leq 100\ \text{km s}^{-1}$ . Similar to F11119+3257, F05189-2524 shows a slight decrement in the flux of molecular lines in the region closest to the quasar which we attribute to a PSF subtraction artifact.

Again using S(5) and the same methods as in F11119+3257, we calculate  $v_{\text{circ}} = 110\ \text{km s}^{-1}$  and a  $v_{\text{esc}} = 330\ \text{km s}^{-1}$ . We improve these estimates by using the absolute H-band magnitude of the host galaxy from (Veilleux et al. 2006) to estimate the stellar luminosity of F05189-2524. Then, assuming a Milky Way-like structure, we scale up Milky Way rotational velocities by the square of the galaxy luminosity ratio and estimate  $v_{\text{circ}} = 120\ \text{km s}^{-1}$  and  $v_{\text{esc}} \simeq 360\ \text{km s}^{-1}$  for F05189-2524.

For both sources, the fit maps from molecular lines not shown in Figure 6 show slight variations in spatial extent and velocities compared to the S(3) and S(5) lines, but the general conclusions are consistent with the results described above.

To explore the decrement of molecular gas in the nuclear region of both sources, we compare the strength of spectrally adjacent low-velocity molecular and ionized gas lines in the same sub-bands. Figure 7 shows the flux ratio of  $\text{H}_2$  S(5) to [Ar II]  $6.99\ \mu\text{m}$  and  $\text{H}_2$  S(2) [Ne II]  $12.81\ \mu\text{m}$  in log scale. Both sources show an increase in the strength of molecular lines relative to the ionized emission lines as the distance from the central quasar increases. The molecular gas lines are 100 times weaker in the nuclear region than they are in the circumnuclear region relative to the ionized lines. This is strong evidence for AGN suppression of molecular gas and thus star formation in the nuclear region.

#### 4.2.2. High Velocity

While the nuclear and low-velocity extended emission of both sources is remarkably similar, the high-velocity extended emission is where they begin to differ in our data. F05189-2524 shows clear evidence of high-velocity extended emission of high IP emission lines, while F11119+3237 shows no such evidence. The strongest evidence for this emission is seen in neon emission lines. We see no high-velocity extended emission in any of the other MIR fine structure lines.

For F05189-2524 we run full cube `q3dfit` analysis on [NeVI]  $7.65\ \mu\text{m}$ , [NeV]  $14.32\ \mu\text{m}$ , and [NeIII]  $15.56\ \mu\text{m}$

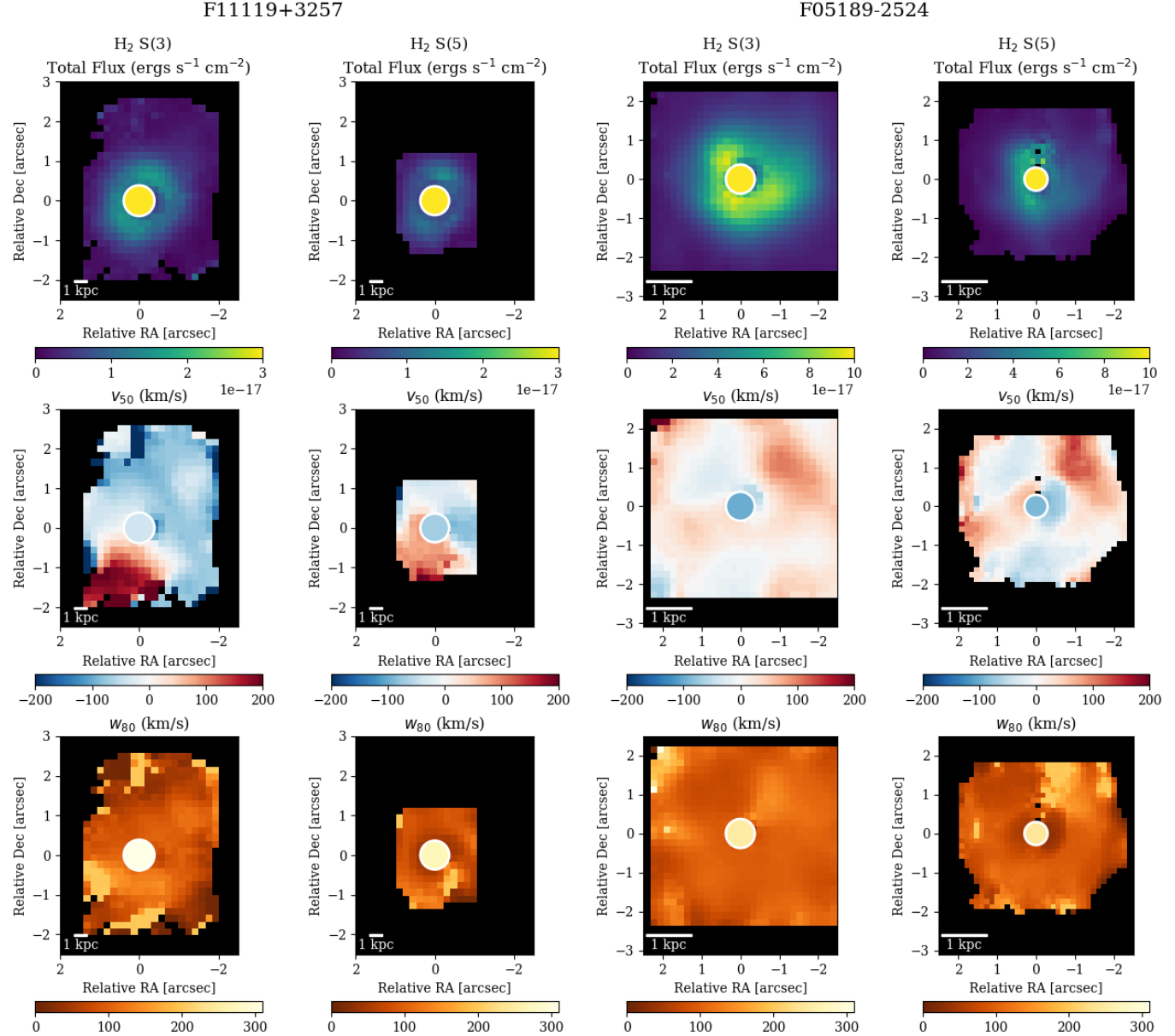


**Figure 6.** Flux and kinematic maps of two molecular lines  $\text{H}_2 0 - 0 \text{ S}(3)$  and  $\text{S}(5)$  from the MIRI/MRS data cubes of both sources. The two left columns correspond to the emission from F11119+3257, and the two right columns correspond to the emission from F05189-2524. Each column shows maps of the emission line flux after processing with `q3dfit` (quasar and stellar continuum emission removed), 50-percentile (median) velocities,  $v_{50}$ , and 80-percentile line widths,  $w_{80}$ , from top to bottom. Fits with a peak flux  $\leq 1\sigma$  have been removed from the result. The white-outlined dot marks the quasar center with a size of the PSF FWHM. The color of the dot represents the corresponding parameter value fit in the nuclear spectrum.

$\mu\text{m}$ . We detect no significant outflowing emission in the  $[\text{Ne II}] 12.81 \mu\text{m}$  line likely caused by the low velocities and contaminating PAH emission in the blue emission wing. In all of the neon lines, there is a dramatic shift of  $\sim 2000 \text{ km s}^{-1}$  from blueshifted emission in the north to redshifted emission in the south. `q3dfit` is unable to range over such large velocities freely and is prone to fitting noise or missing components entirely when both the redshifted and blueshifted components are fit at the

same time. To allow for reliable fitting and to reduce noise in the results, we only fit blueshifted emission to the north of the quasar and redshifted emission to the south. We do not see any significant redshifted emission to the north or blueshifted emission to the south that is being ignored by these methods. Using test fits of spaxels in both regions, we set initial guesses on the velocity, width, and number of Gaussian components for all lines. We fit two components to  $[\text{Ne VI}]$  and  $[\text{Ne III}]$  and only

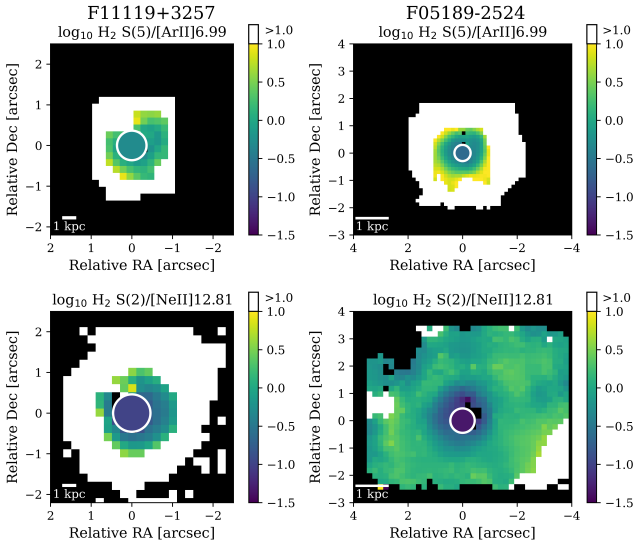


**Figure 7.** Emission line flux (quasar and stellar continuum emission removed) ratio of  $\text{H}_2 \text{ S}(5)/[\text{Ar II}]$  (top row) and  $\text{H}_2 \text{ S}(2)/[\text{Ne II}]$  12.81 (bottom row) for F11119+3257 (left column) and F05189-2524 (right column). White pixels show regions with a ratio greater than 1, where molecular lines were fit, but ionized lines were not. Black pixels show regions where neither molecular nor ionized lines were fit. The white-outlined dot marks the quasar center with a size of the PSF FWHM. The color of the dot represents the corresponding parameter value fit in the nuclear spectrum.

one component to [Ne V] in our fits to the extranuclear emission.

The flux and kinematic maps resulting from this fitting are shown in Figure 8. When multiple components are fit to the outflow, as in the case of [Ne VI], we combine them and calculate the flux,  $v_{50}$ , and  $w_{80}$  for the combined complex. Examples of the kinematic spectral fits in the redshifted and blueshifted regions for both lines and [Ne III] are shown in Figure 9.

A high-velocity,  $|v_{50}| \sim 1000 \text{ km s}^{-1}$ , biconical emission is seen in all three neon emission lines in Figure 8. This is well beyond the expected rotational velocity of the host galaxy ( $\sim 150 \text{ km s}^{-1}$ ), and thus we classify it as an outflow. The general direction and velocities of this outflow are consistent with the visible [N II] 6585 Å measurements (Rupke et al. 2017). CO measurements seem to show the same directionality as our outflow (Fluetsch et al. 2019; Lutz et al. 2020), although recent measurements from Lamperti et al. (2022) are not as decisive. All resolved molecular outflow detections show a strong redshifted component but very weak blueshifted component contradictory with our results. Similar to the nuclear emission, the outflow has a higher velocity in higher ionization stages, with a flux-weighted mean  $v_{50}$  ranging from  $500 \text{ km s}^{-1}$  in [Ne III] to  $810 \text{ km s}^{-1}$  in [Ne VI]. The

data also show that the spatial extent of the outflow decreases in higher states, as the flux-weighted mean outflow radius  $R_{\text{out}}$  decreases from 1060 pc in [Ne III] to 860 pc in [Ne VI]. Consistent with observations of another Seyfert 2 galaxy NGC 7319 (Pereira-Santaella et al. 2022), and with a spatially stratified outflow as discussed in Section 4.1.

The blueshifted outflow for all lines typically peaks at a slightly lower velocity ( $\sim 100 \text{ km s}^{-1}$ ) than the unresolved emission and lacks an extended blueshifted tail. For the redshifted side [Ne III] and [Ne V] are easily fit with a single Gaussian component, but [Ne VI] shows two distinct clumps at  $v_{50} \sim 500 \text{ km s}^{-1}$  and  $v_{50} \sim 1500 \text{ km s}^{-1}$ . A low-velocity component, likely due to disk rotation, is also clearly visible, and fit, in [Ne III] but hard to quantify. In fitting of the redshifted outflow region, the quasar template often overfits the PSF emission. This can be seen in the bottom left and top left panels of Figure 9 and only has a minor effect, slightly reducing derived masses.

For F11119+3257, we attribute the lack of detection of a resolved outflow to the greater distance to the source. The brightest portion of the [Ne III] outflow in F05189-2524 is  $\leq 1 \text{ kpc}$  from the quasar, which is the effective size of the PSF FWHM at that wavelength for F11119+3257, making the outflow difficult to resolve. This, in combination with the weaker [Ne III] emission in F11119+3257, makes resolved kpc-scale outflows unlikely to be observed with MIRI MRS. Still, given the similarity of the two sources and the strong unresolved warm ionized outflow, and errors involved, we cannot rule out the presence of a kpc-scale outflow in the source.

## 5. DISCUSSION

### 5.1. Dust

The ratios between the different PAH features may be a good indicator of the PAH grain size, PAH ionization level, and incident radiation field on those PAHs (Rigopoulou et al. 2021; Maragkoudakis et al. 2020; Draine et al. 2021). In Figure 10, we plot measured PAH fluxes from Table 1 against PAH model grids from Rigopoulou et al. (2021) and a sample of Seyfert galaxies from García-Bernete et al. (2022a) and Seyfert and star forming galaxies from Rigopoulou et al. (2024) and García-Bernete et al. (2022b). For both sources, we find that F05189-2524 and F11119+3257 show evidence of a smaller ratio of 11.3 to 7.7 PAH than the Seyfert galaxies. This could either be explained by these sources having a more ionized PAH species or a PAH species under a stronger incident radiation field than the Seyfert galaxies. Additionally, we see that stronger ratios of 11.3 PAH and 6.2 PAH to the 7.7 PAH feature in F11119+3257,

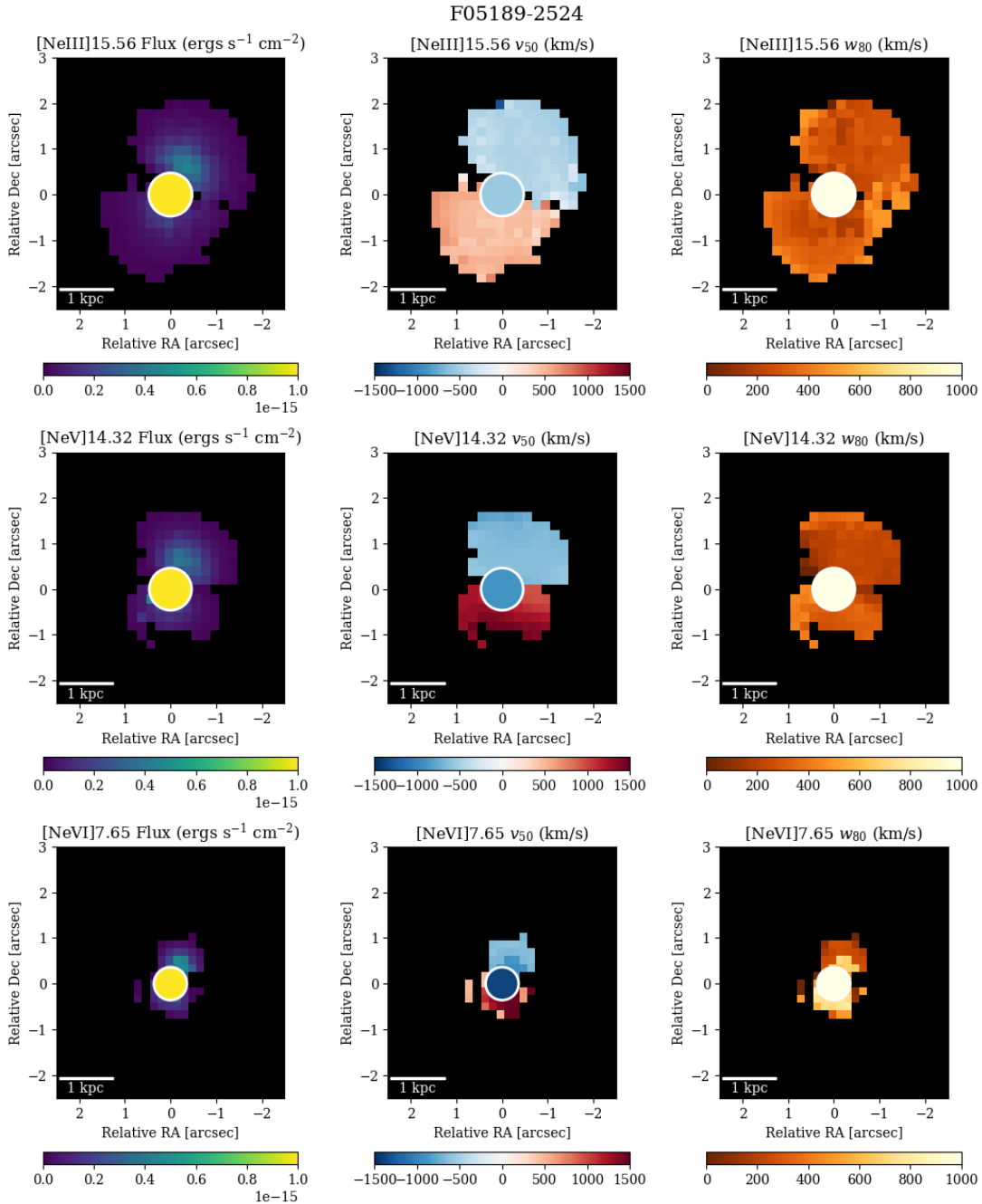


**Figure 8.** Flux and kinematic maps of three ionized lines [Ne III] 15.56  $\mu\text{m}$  (top row), [Ne V] 14.32  $\mu\text{m}$  (middle row), and [Ne VI] 7.65  $\mu\text{m}$  (bottom row) from the MIRI/MRS data cube for F05189-2524. Each row shows maps of the emission line flux after processing with `q3dfit` (quasar and continuum emission removed), 50-percentile (median) velocities,  $v_{50}$ , and 80-percentile line widths,  $w_{80}$ , from left to right. Fits with a peak flux  $\leq 3\sigma$  have been removed from the result. The white-outlined dot marks the quasar center with a size of the PSF FWHM. The color of the dot represents the corresponding parameter value fit in the nuclear spectrum.

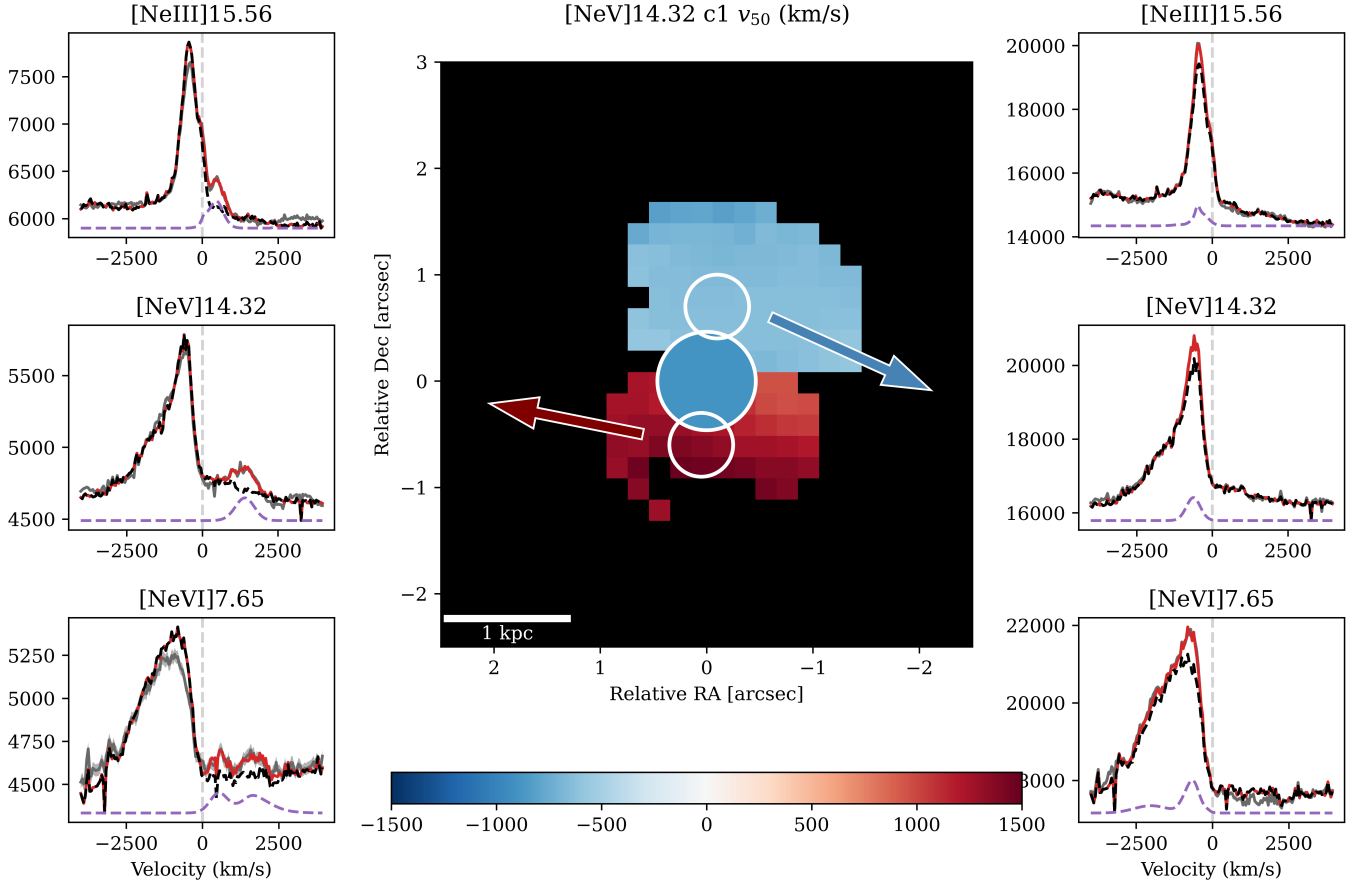


**Figure 9.** Examples of extracted spectra for three ionized lines,  $[\text{Ne III}]$   $15.56 \mu\text{m}$ ,  $[\text{Ne V}]$   $14.32 \mu\text{m}$ , and  $[\text{Ne VI}]$   $7.65 \mu\text{m}$ , from the redshifted (left column) and blueshifted (right column) regions of the F05189-2524 spectral cube. The central map depicts the excess emission  $v_{50}$  of  $[\text{Ne V}]$ . Emission from the other two lines has been extracted for each marked circle from the corresponding spatial region of their respective cubes. Fits with a peak flux  $\leq 3\sigma$  have been removed from the result. White unfilled circles mark the regions where spectra have been extracted from the redshifted (south of the quasar) and blueshifted (north of the quasar) emission regions. In the extracted spectra subplots, the red line is the sum of the scaled quasar template and the line fit, the latter of which is shown as the purple dashed line and the former of which is shown as the black dashed line. The data are the dark gray line (often hidden behind the red line) with the  $1-\sigma$  error range filled in with the lighter gray. The y-axis units are  $10^{-16} \text{ erg s}^{-1} \text{ cm}^{-2} \mu\text{m}^{-1}$ .

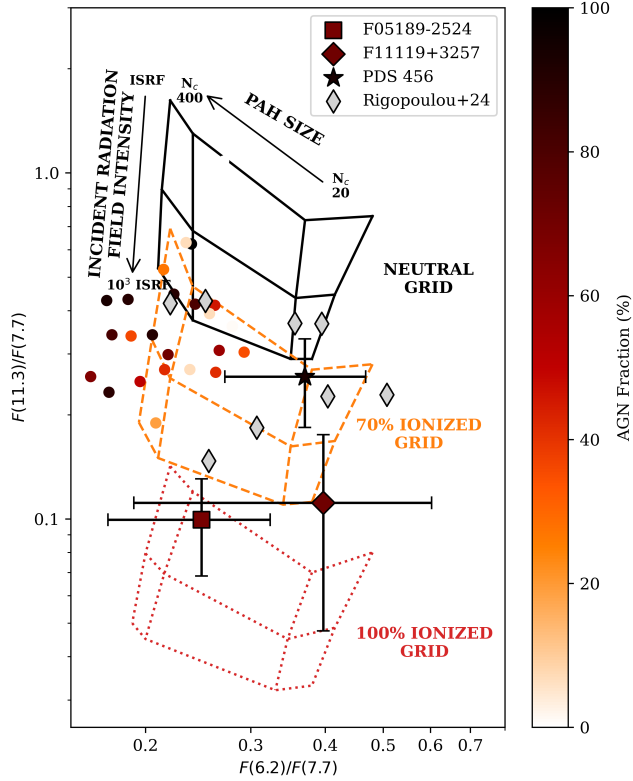


**Figure 10.** PAH ratio diagnostic diagram. Flux ratios of the PAH 6.2/7.7  $\mu\text{m}$  and PAH 11.3/7.7  $\mu\text{m}$  from Table 1. The grids are estimated from Rigopoulou et al. (2021). They correspond to mixtures of PAH species ionized to various levels (0%, 70%, and 100 % ionized PAH molecules). The individual grids range from softer ( $1 \times$  Interstellar Radiation Field (ISRF); top of the grid) to harder ( $10^3 \times$  ISRF; bottom of the grid) incident radiation fields and from smaller ( $N_c = 20$ , the number of carbon atoms; right side of the grid) to larger ( $N_c = 400$ ; left side of the grid) PAHs. The colored circles are PAH ratios for Seyfert galaxies colored by their MIR AGN fraction as defined in García-Bernete et al. (2022a). Values for F11119+3257, F05189-2524, and PDS 456 (Seebeck et al. 2024) are plotted with error bars, and the color reflects their measured AGN contribution (Veilleux et al. 2009a; Seebeck et al. 2024). JWST observations of Seyfert and star-forming galaxies from Rigopoulou et al. (2024) are represented by the thin gray diamonds with the inclusion of NGC 6552 from García-Bernete et al. (2022b).

compared to those ratios in F05189-2524, are indicative of a smaller and less ionized PAH species. However, large errors in the measurements make conclusions indefinite.

The MIR PAH features are ubiquitous in galactic and extragalactic sources. These features are strongly correlated with SFR in normal non-active galaxies (Peeters et al. 2004; Shipley et al. 2016; Li 2020). However, AGN suppression of PAH features can affect the SFR-LPAH relation. This is done through the destruction of

PAH molecules (Voit 1992; Siebenmorgen et al. 2004). The 11.3  $\mu\text{m}$  PAH feature is arguably the least AGN-suppressed PAH feature in our observations and can fairly reliably indicate SFR for galaxies with AGN (Diamond-Stanic & Rieke 2012; Shipley et al. 2016).

Thus we use Equation 2 from Diamond-Stanic & Rieke (2012) to derive  $\text{SFR} = 6 \pm 2 \text{ M}_\odot \text{ yr}^{-1}$  for F11119+3257 and  $\text{SFR} = 4 \pm 2 \text{ M}_\odot \text{ yr}^{-1}$  for F05189-2524. We find these results on the lower end of other SFR-LPAH relations using the other PAH features (6.2  $\mu\text{m}$  and 7.7  $\mu\text{m}$ ) and calibration samples (Farrah et al. 2007; Pope et al. 2008; Lutz et al. 2008; Treyer et al. 2010; Shipley et al. 2016); which range from  $4 - 114 \text{ M}_\odot \text{ yr}^{-1}$  for F11119+3257 and  $4 - 81 \text{ M}_\odot \text{ yr}^{-1}$  for F05189-2524. We attribute this large range to variations in PAH-SFR relation calibration samples and methods, see Shipley et al. 2016 for a more detailed discussion. For F11119+3257, the high-end results from this analysis are consistent with the SFR estimated from FIR dust emission  $190 \pm 90 \text{ M}_\odot \text{ yr}^{-1}$  (Pan et al. 2019).

## 5.2. Molecular Gas

To each spaxel in the unified cube fits, using emission probabilities for the  $\text{H}_2$   $v = 0 - 0$  transitions from Roueff et al. (2019) and Equation 1 of Youngblood et al. (2018) to calculate  $N(\nu_u, J_u)$ , we construct an excitation diagram for all of the  $\text{H}_2$   $0 - 0$  lines present in the spaxel. We then implement two methods to determine the temperature and column density of the molecular gas. We provide an example fit using both of these methods in Figure 11 using the data from the nuclear emission.

The first method uses Equation 2 from Youngblood et al. (2018),

$$\log_{10} \frac{N(\nu_u, J_u)}{g(J_u)} = -\frac{1}{T \cdot \ln(10)} \frac{E(\nu_u, J_u)}{k_B} + \log_{10} N(0, 0), \quad (1)$$

to construct a two-component linear fit of the data. The first component fits lines sensitive to cooler temperatures (S(1), S(2), S(3);  $T_{cool}$ ) and the second component fits only the lines sensitive to hotter temperatures (S(4), S(5), S(6), S(7), S(8);  $T_{warm}$ ). We use the column densities of the mass-dominant, cooler molecular gas to calculate the per-spaxel  $\text{H}_2$  gas mass. This broken linear fit can be seen as the blue (cold) and red (warm) lines in Figure 11.

The second method uses an adapted Python implementation from Jones et al. (2024) of the  $\text{H}_2$  excitation model of Togi & Smith (2016) to fit the molecular data. The Togi & Smith (2016) model assumes a power-law distribution for rotational molecular emission lines and fits the lower bounds on the temperature distribution  $T_l$  and the power law slope. These, in combination with an

assumed upper bound on the temperature distribution ( $T_u = 2000$  K; the model is insensitive to any values larger than 2000 K), allow for the total column density and mass of  $H_2$  to be fit. This power law fit can be seen as the gray solid line in Figure 11.

We note that the Togi & Smith (2016) method can better extrapolate the  $S(0)$  flux, which is unobservable with MIRI and an indicator of cooler, more abundant gas. This causes the method to provide consistently greater column densities and lower temperature estimates than the broken linear method, but we are unable to consistently quantify this difference across varying spaxels in order to apply a correction.

In all spaxels and the nuclear fit, we assume an ortho/para ratio of 3 for the statistical weights of the molecular transitions. Smaller ortho/para ratios have been observed in some cases (e.g. Habart et al. 2005), but a value of 3 is a conservative upper limit useful for comparisons, and we generally find that lower values cause a discontinuity between the ortho and para transitions.

In the nuclear region, we see a significant drop in the  $S(3)$  line relative to other nearby lines. We attribute this to extinction from the silicate absorption feature from  $\tau_{9.7}$ . We correct this by fitting the Togi & Smith (2016) method with all lines excluding  $S(3)$ , correcting  $S(3)$  to the Togi & Smith (2016) fit, and refitting the broken linear method. The uncorrected  $S(3)$  line is shown in light gray in Figure 11 while the corrected version is shown in black. Outside of the nucleus, we see no significant signs of extinction and lack the data quality to consistently determine and correct for it. Thus, we do not correct the  $H_2$   $S(3)$  line for extinction in our extranuclear fits.

From our full cube fitting, we find that the Togi & Smith (2016) power-law method is very susceptible to fitting errors with this data. This occurs largely in the  $H_2$   $S(1)$  line caused by nearby fringing or residual noise and can lead to unphysically high column densities and low temperatures. In addition, the lower signal  $S(4) - S(7)$  lines often confound the fitting. We find that the simple linear fit to colder warm molecular gas is more robust in response to fitting errors and does not require the weaker  $S(4) - S(7)$  lines.

This leads us to use the linear fit on the lines sensitive to cooler temperatures ( $S(1)$ ,  $S(2)$ ,  $S(3)$ ) in our full temperature and column density maps shown in Figure 12. To make these maps, we only fit spaxels where all three lines are present above  $1-\sigma$  as depicted by the white region in the right column of Figure 12. We display the nuclear fitting results as a circle with the size PSF FWHM and colored based on the nuclear temperature and column density. Both sources show higher column

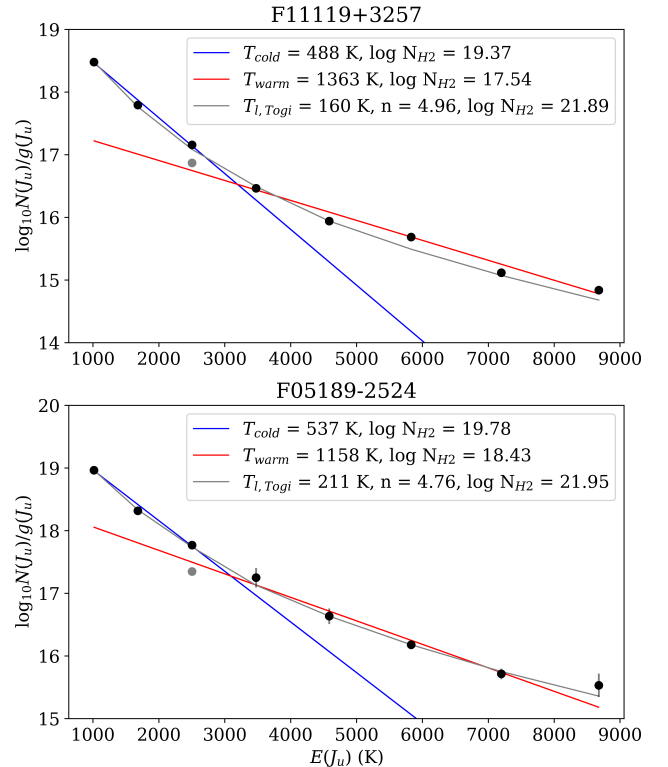


**Figure 11.** Excitation diagram for the rotational transitions of  $H_2$  for F11119+3257 (top) and F05189-2524 (bottom) extracted from the nuclear spectrum. Values of  $g(J_u)$ ,  $E(J_u)$ , and  $A$  were gathered from Roueff et al. (2019) in order to convert from line intensities to  $N(J_u)$ . We fit the data points with two methods: one using two-component (warm and cold) linear regression and two a power-law distribution based on the model in Togi & Smith (2016). The uncorrected for extinction emission for  $H_2$  is represented by the gray point, and the corrected emission by the black point.

density and temperature in the nuclear region as compared to the extended emission. In F11119+3257, we see no significant spatial trends in temperature or column density. In F05189-2524, we note that the broad, slightly redshifted clump to the northwest shown in Figure 6 is spatially correlated with a slight decrease in column density with respect to nearby regions.

Using the column density results from both the unresolved and resolved cases, we can extract a total mass in warm molecular gas by multiplying by the total area uniquely subtended by the unresolved and resolved emission and the mass of a  $H_2$  molecule. For F05189-2524, we derive a mass of  $M_{H2}^{warm} = 4.5 \pm 1 \times 10^8 M_\odot$  with 1.3% of the mass unresolved. This makes up  $\sim 3\%$  of the cold molecular mass traced by CO line emission (Fluetsch et al. 2019; Lutz et al. 2020; Lamperti et al. 2022). For F11119+3257, we derive a mass of  $M_{H2}^{warm} = 3.0 \pm 1 \times 10^8 M_\odot$  with 0.2% of the mass unresolved. This makes up

~3% of the cold molecular mass traced by CO line emission (Veilleux et al. 2017). For both sources, we find our results in line with previous measurements of  $M_{H2}^{warm}$  (Veilleux et al. 2009a; Pereira-Santaella et al. 2014) and the comparison between warm and cold molecular gas (Rigopoulou et al. 2002; Pereira-Santaella et al. 2014).

### 5.3. Ionized Gas

We use the luminosities of the outflowing neon-emitting gas to estimate the mass of the warm ionized outflow from our data. For every spaxel, we take the fit of the extranuclear component and sum all of the flux with absolute velocities greater than  $300 \text{ km s}^{-1}$ , then convert the total flux of the outflow into a luminosity using the luminosity distance  $D_L$ . We choose  $\pm 300 \text{ km s}^{-1}$  as a cutoff because it is beyond the observed projected disk rotational velocities from rotational hydrogen lines ( $v_{\text{circ}} \sim 110 \text{ km s}^{-1}$  for F05189-2524 and  $130 \text{ km s}^{-1}$  for F11119+3257). For the unresolved outflow component, we apply the same method to the fit of the nuclear spectrum. Then subtract the flux from the extranuclear emission so that it is not double-counted.

Next, the nuclear and extranuclear line luminosities are used to estimate the mass in warm ionized gas, following a method similar to that in Seebeck et al. (2024), except we use gas in the  $\text{Ne}^{1+}$ ,  $\text{Ne}^{4+}$ , and  $\text{Ne}^{5+}$  states in addition to the  $\text{Ne}^{2+}$  state. We determine the amount of ionized gas explained by the emission of each neon species, then sum them together for a total warm ionized gas mass. To do this we assume four things: 1) the outflowing neon emission is only concentrated in these four states; 2)  $n_{\text{H}} = 10 \times n_{\text{He}}$ ; 3) a solar neon abundance of  $[\text{Ne}/\text{H}] = -3.91$  (Nicholls et al. 2017); and 4) line emissivities calculated from PyNeb (Luridiana et al. 2015) (assuming constant  $T = 10^4 \text{ K}$ , which is appropriate for AGN photoionized gas, and constant  $n_e = 10^3 \text{ cm}^{-3}$  consistent with measurements in Rupke et al. 2017). This results in

$$M_{\text{ionized}}^{[\text{NeII}]} = 6.09 \times 10^8 \frac{C L_{44}([\text{Ne III}])}{\langle n_{e,3} \rangle 10^{[\text{Ne}/\text{H}]}} M_{\odot}, \quad (2)$$

$$M_{\text{ionized}}^{[\text{NeIII}]} = 2.96 \times 10^8 \frac{C L_{44}([\text{Ne III}])}{\langle n_{e,3} \rangle 10^{[\text{Ne}/\text{H}]}} M_{\odot}, \quad (3)$$

$$M_{\text{ionized}}^{[\text{NeV}]} = 2.99 \times 10^7 \frac{C L_{44}([\text{Ne V}])}{\langle n_{e,3} \rangle 10^{[\text{Ne}/\text{H}]}} M_{\odot}, \quad (4)$$

$$M_{\text{ionized}}^{[\text{NeVI}]} = 4.17 \times 10^7 \frac{C L_{44}([\text{Ne VI}])}{\langle n_{e,3} \rangle 10^{[\text{Ne}/\text{H}]}} M_{\odot}, \quad (5)$$

where  $C \equiv \langle n_e \rangle^2 / \langle n_e^2 \rangle$  is the electron density clumping factor, which we assume is of order unity,  $L_{44}$  is the neon luminosity normalized to  $10^{44} \text{ erg s}^{-1}$ ,  $\langle n_{e,3} \rangle$  is the

average electron density normalized to  $10^3 \text{ cm}^{-3}$ . As mentioned earlier, the mass from this estimate assumes a constant temperature  $T \sim 10^4 \text{ K}$ , but note that the temperature dependence is weak. It also assumes that the electron densities are below the critical densities<sup>3</sup> so that collisional de-excitation is unimportant. Summing these individual components gives the final derived ionized gas mass

$$M_{\text{ionized}} = M_{\text{ionized}}^{[\text{NeII}]} + M_{\text{ionized}}^{[\text{NeIII}]} + M_{\text{ionized}}^{[\text{NeV}]} + M_{\text{ionized}}^{[\text{NeVI}]} \quad (6)$$

For each spaxel, we then use these calculated masses, the pixel scale  $\Delta r$ , and the outflow velocity  $v_{\text{out}} \cong v_{50} + \sigma \sim v_{84}$  to roughly estimate the mass outflow rate,

$$\dot{M}_{\text{out}} = \frac{M_{\text{out}} v_{\text{out}}}{\Delta r}, \quad (7)$$

momentum outflow rate,

$$\dot{P}_{\text{out}} = \dot{M}_{\text{out}} v_{\text{out}}, \quad (8)$$

and outflow power,

$$\dot{E}_{\text{out}} = \frac{1}{2} \dot{M}_{\text{out}} v_{\text{out}}^2. \quad (9)$$

For the nuclear emission, the FWHM/2 of the PSF is used as an upper limit on the  $\Delta r$ , and the rest of the calculation is the same. Once these energetics are calculated for each spaxel, the results for each neon state and the total warm ionized gas are summed, calculated, and presented in Table 3. For F11119+3257, we calculate masses only for the unresolved nuclear emission, but in F05189-2524, we calculate masses for both the resolved and unresolved emission. In addition, Table 3 includes the outflow radius  $R_{\text{out}}$ , outflow velocity  $v_{\text{out}}$ , and compiled results from other papers displaying the outflow energetic calculations from other species of gas derived at a wide variety of distances for both sources. For resolved emission, the flux weighted mean for all spaxels is reported.

In the unresolved measurements of the neon gases, we measure that F11119+3257 has over twice the mass of outflowing gas ( $\sim 7 \times 10^6 M_{\odot}$ ) as F05189-2524 ( $\sim 3 \times 10^6 M_{\odot}$ ). When only considering mass derived from  $[\text{Ne V}]$  values, our measurements are greater than all of those measured in a sample of Seyfert galaxies from

<sup>3</sup>  $n_{\text{crit}}([\text{Ne II}]) = 6.3 \times 10^5 \text{ cm}^{-3}$   
 $n_{\text{crit}}([\text{Ne III}]) = 2.1 \times 10^5 \text{ cm}^{-3}$   
 $n_{\text{crit}}([\text{Ne V}]) = 3.2 \times 10^4 \text{ cm}^{-3}$   
 $n_{\text{crit}}([\text{Ne VI}]) = 6.3 \times 10^5 \text{ cm}^{-3}$

**Table 3.** Outflow Parameters

Ref	Gas Phase	Tracer	Component	$M_{\text{out}}$ ( $10^5 M_{\odot}$ )	$v_{\text{out}}$ ( $\text{km s}^{-1}$ )	$R_{\text{out}}$ (pc)	$\dot{M}_{\text{out}}$ ( $M_{\odot} \text{yr}^{-1}$ )	$\dot{P}_{\text{out}}$ ( $10^{33} \text{dyn}$ )	$\dot{E}_{\text{out}}$ ( $10^{41} \text{erg s}^{-1}$ )
(1)	(2)	(3)	(4)	(5)	(6)	(7)	(8)	(9)	(10)
F11119-2524									
(1)	Warm Ionized	[Ne II]	12.81	Unresolved	$29.4^{+1.6}_{-1.6}$	$1300^{+100}_{-100}$	960	$4.0^{+0.2}_{-0.2}$	$31.8^{+1.8}_{-1.8}$
(1)		[Ne III]	15.56	Unresolved	$36.7^{+2.5}_{-2.5}$	$1700^{+100}_{-100}$	1150	$5.1^{+0.4}_{-0.4}$	$53.8^{+4.3}_{-4.3}$
(1)		[Ne V]	14.32	Unresolved	$1.8^{+0.3}_{-0.3}$	$1900^{+200}_{-200}$	1050	$0.3^{+0.06}_{-0.06}$	$3.9^{+0.7}_{-0.7}$
(1)		[Ne VI]	7.65	Unresolved	$6.0^{+3.3}_{-3.3}$	$3100^{+400}_{-400}$	670	$2.8^{+1.8}_{-1.8}$	$53.5^{+36.1}_{-36.1}$
(1)			Total	$73.88^{+5.5}_{-5.5}$			$12.1^{+1.8}_{-1.8}$	$143.1^{+18.5}_{-18.5}$	$151.3^{+27.1}_{-27.1}$
(2)	Hot Ionized	Fe K	Unresolved	—	75900	$2.3 \times 10^{-5}$	0.5-2	240-1000	9100-38000
(3)	Neutral	Na I D	Unresolved	0.05	1000	10	0.59	25	13
(4)	Cold Molecular	OH	Unresolved	$2350^{+2700}_{-1100}$	$1000^{+200}_{-200}$	300	$800^{+1200}_{-550}$	$5500^{+7050}_{-3750}$	$2750^{+4780}_{-2050}$
(5)	Cold Molecular	CO (1-0)	Unresolved	6000-14000	$1000^{+200}_{-200}$	4000-15000	80-200	750-1500	300-900
F05189-2524									
(1)	Warm Ionized	[Ne II]	12.81	Unresolved	$9.00^{+0.24}_{-0.24}$	$700^{+60}_{-60}$	240	$2.73^{+0.27}_{-0.27}$	$12.16^{+1.69}_{-1.69}$
(1)			Resolved	—	—	—	—	—	—
(1)		[Ne III]	15.56	Unresolved	$14.19^{+0.67}_{-0.67}$	$950^{+80}_{-80}$	270	$5.11^{+0.65}_{-0.65}$	$30.46^{+5.29}_{-5.29}$
(1)			Resolved	$1.45^{+0.34}_{-0.34}$	$700^{+625}_{-360}$	$1060^{+1010}_{-950}$	$0.61^{+0.14}_{-0.14}$	$3.06^{+0.71}_{-0.71}$	$1.37^{+0.36}_{-0.36}$
(1)		[Ne V]	14.32	Unresolved	$1.94^{+0.24}_{-0.24}$	$1600^{+199}_{-100}$	250	$1.25^{+0.12}_{-0.12}$	$12.50^{+1.48}_{-1.48}$
(1)			Resolved	$0.14^{+0.03}_{-0.03}$	$920^{+880}_{-850}$	$710^{+1190}_{-620}$	$0.07^{+0.02}_{-0.02}$	$0.42^{+0.10}_{-0.10}$	$0.19^{+0.05}_{-0.05}$
(1)		[Ne VI]	7.65	Unresolved	$2.25^{+0.83}_{-0.83}$	$2000^{+200}_{-200}$	170	$2.73^{+0.99}_{-0.99}$	$34.78^{+13.35}_{-13.35}$
(1)			Resolved	$0.13^{+0.04}_{-0.04}$	$1430^{+1350}_{-1000}$	$860^{+600}_{-410}$	$0.11^{+0.03}_{-0.03}$	$1.24^{+0.32}_{-0.32}$	$1.24^{+0.31}_{-0.31}$
(1)			Total	$30.27^{+2.09}_{-2.09}$			$12.61^{+1.92}_{-1.92}$	$84.62^{+18.94}_{-18.94}$	$66.62^{+18.22}_{-18.22}$
(6)	Hot Ionized	Fe K	Unresolved	—	33000	0.002-0.01	1-6.3	220-1300	3600-21500
(7)	Hot Ionized	Fe K	Unresolved	—	$22800-42900$	0.0029-0.0043	20.0	4400	80000
(8)	Cold Molecular	OH	Unresolved	$1890^{+2700}_{-1100}$	200-550	170-340	$270^{+22}_{-130}$	$680^{+130}_{-290}$	$160^{+40}_{-70}$
(9)	Cold Molecular	CO (3-2)	Resolved	7400	491	189	219	680	170
(10)	Cold Molecular	CO (2-1)	Resolved	$460^{+10}_{-10}$	$294^{+16}_{-16}$	$830^{+10}_{-10}$	$16.6^{+0.4}_{-0.4}$	$31^{+5}_{-4}$	$9^{+4}_{-4}$
(11)	Cold Molecular	CO (1-0)	Resolved	741	446	1052	32.56	91	20.4
(12)	Neutral	Na I D	Resolved	$3800^{+270}_{-170}$	560	3000	$95^{+12}_{-6}$	$590^{+90}_{-40}$	$380^{+70}_{-30}$
(12)	Warm Ionized	[N II]	Resolved	$230^{+34}_{-63}$	423	3000	$2.5^{+0.5}_{-0.7}$	$7.7^{+1.4}_{-2.1}$	$2.1^{+0.4}_{-0.5}$

NOTE—Meaning of the columns: (1) Reference, (2) Gas phase of the outflow, (3) emission line tracer used to derive the mass, (4) component of the outflow, either resolved or unresolved, (5) mass of the outflowing gas phase, (6) typical  $v_{50}$  velocity of the outflow, (7) median radius of the outflow, (8) mass outflow rate, (9) momentum outflow rate, and (10) energy outflow rate

**References**—(1) This paper, (2) Tombesi et al. (2017), (3) Rupke et al. (2005), (4) Tombesi et al. (2015), (5) Veilleux et al. (2017), (6) Smith et al. (2019), (7) Noda et al. (2025), (8) González-Alfonso et al. (2017), (9) Fluetsch et al. (2019), (10) Lamperti et al. (2022), (11) Lutz et al. (2020), (12) Rupke et al. (2017)

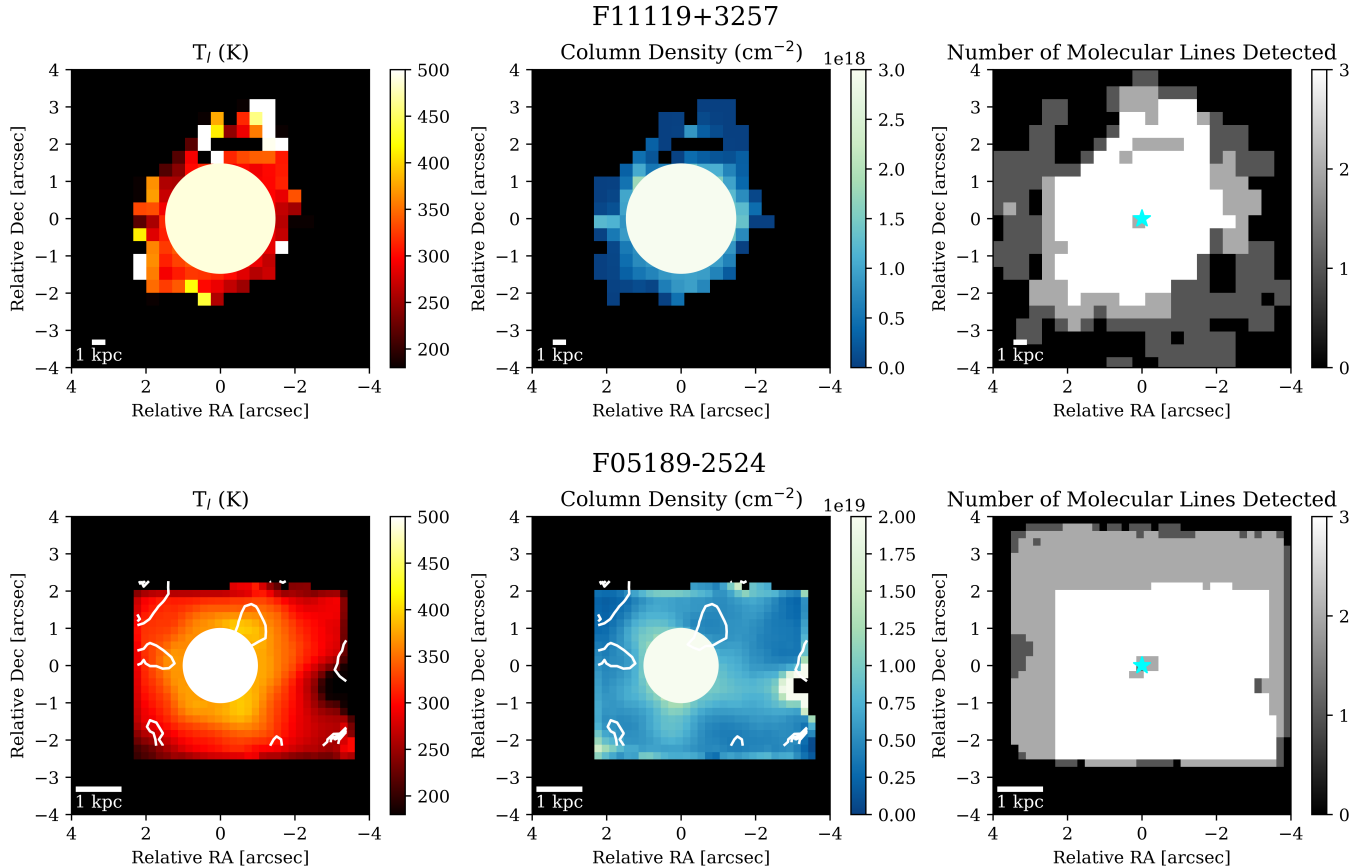


**Figure 12.** Maps of the temperature (K; left column), column density ( $\text{cm}^{-2}$ ; center column), and number of molecular lines detected (right column) in F11119+3257 (top row) and F05189-2524 (bottom row). Temperatures and column densities are determined using a linear fit to the rotational  $\text{H}_2$  lines sensitive to cooler temperatures (S(1), S(2), S(3)). Only spaxels where all three lines are present are fit. The central circles in the left and center columns mark the quasar center with a size of the PSF FWHM and color of the corresponding parameter value. The white contour in the temperature and column density maps of F05189-2524 traces the velocity width of the extended  $\text{H}_2$  S(3) emission shown in Figure 6

the GATOS sample (Zhang et al. 2024). Our ionized mass outflow rates are slightly lower than those expected from empirical relations based on the AGN luminosity from Fiore et al. (2017), but well within the observed scatter. In the breakdown between different ionization states, lower states ([Ne II] and [Ne III]) represent the largest phases in mass, representing  $\sim 85\%$  of the outflow mass; however, the high velocities of the [Ne V] and [Ne VI] states make them a significant component of the momentum ( $\sim 45\%$ ) and energetic ( $\sim 65\%$ ) outflow rates. Based on our measurements of escape velocity for both sources discussed in Sections 4.2.1 we estimate that  $\sim 90\%$  of the outflowing mass in both sources will escape the galaxy up to a distance of  $33 R_{\text{out}}$ . This is a very significant portion of the outflowing mass that will be driven to enrich the circumgalactic medium but still a relatively small component of the overall galaxy mass. Below, we compare the emission of both sources to different gas phases at varying distance scales and resolution.

For F11119+3257, we can see that the warm ionized gas makes up a relatively small component of the larger-scale outflow. Compared to both the instantaneous 300 pc measurements of OH ( $\sim 2350 M_{\odot}$ ; Tombesi et al. 2015) and the time-averaged kpc scale measurements of CO(1-0) ( $\sim 10000 M_{\odot}$ ; Veilleux et al. 2017), the mass in warm ionized gas represents  $\sim 3\%$  and  $\sim 1\%$  of the outflowing cold molecular gas. As the outflow velocities are similar between the warm ionized and cold molecular gas measurements our results have no significant impact on the large scale momentum or energy outflow rates. Previous results have shown that momentum is relatively conserved from the AGN, to the UFO, and the Kpc scale outflow (Veilleux et al. 2017; Nardini & Zubovas 2018; Lanzuisi et al. 2024), a conclusion unchanged by these results. Looking at the energy outflow rates, a significant component ( $\sim 5\%$ ) of the AGN luminosity drives the UFO, and  $\sim 30\%$  of that energy is coupled to the larger scale galactic outflow. Showing that the energy from the AGN is relatively inefficient in coupling to the host galaxy but still very significant in its impact.

From the unresolved measurements of F05189-2524, we see a similar picture as F11119+3257: the mass in warm ionized gas in F05189-2524 makes up a relatively insignificant portion of the outflow energetics of the source. And, the resolved component represents an even smaller portion ( $\sim 10\%$  by mass compared to the unresolved component) of the outflow.

Previous results show resolved measurements in cold molecular (González-Alfonso et al. 2017; Fluetsch et al. 2019; Lutz et al. 2020; Lamperti et al. 2022), neutral (Rupke et al. 2017), and warm ionized gases (Rupke

et al. 2017). Results in the cold molecular gas are consistent within an order of magnitude of each other and variations between the different CO measurements are likely explained by variations in methods, instruments, and systematic errors as described in Sections 4.6.1 and 4.6.2 of Lamperti et al. (2022). Regardless of the reference used, the warm ionized gas represents  $\sim 0.5\text{--}5\%$  of the outflowing cold molecular gas mass. Measurements of the neutral gas Rupke et al. (2017) represent another significant component of the outflow, similar in mass, momentum, and energy to the molecular gas. However, there is likely some overlap between these phases of gas.

We note that our resolved warm ionized gas measurements are an order of magnitude smaller than those based on the visible [N II] measurements in Rupke et al. (2017). This result is unlikely to be caused by any differences in metallicity or electron density measurements used in calculations. Instead, it possibly could be caused by emission line flux being attributed to nearby PAH emission or variations in our mass derivation methods compared to those used in Rupke et al. (2017).

For F05189-2524, a sum of the momentum outflow rates from all of these large scale outflow phases ( $\dot{P}_{\text{outer}}$ ) is consistent, given the uncertainties, with momentum conservation ( $\dot{P}_{\text{outer}} \sim \dot{P}_{\text{inner}} \sim L_{\text{bol}}/c$ ) from the initial momentum of the AGN and UFO. The warm ionized gas represents  $\leq 0.1\%$  of this momentum outflow rate. Slightly higher velocities in the warm ionized gas ( $\sim 500 \text{ km s}^{-1}$ ) than the other phases cause it to have a larger impact on the energy outflow rates making up  $\sim 5\%$  of the total rate. Still, the overall picture is largely unchanged, as energy from the AGN is lost as distance from the center increases:  $\sim 5\% L_{\text{AGN}}$  in the sub-pc UFO and  $\sim 0.5\% L_{\text{AGN}}$  in the galactic scale kpc outflow.

Overall, the addition of warm ionized gas measurements to the energetic census of both sources has no significant impact on the outflow energetics, and the conclusions from previous papers remain: the driving energetics of F11119+3257 (Veilleux et al. 2017; Nardini & Zubovas 2018; Lanzuisi et al. 2024) and F05189-2524 (Smith et al. 2019) are broadly consistent with a momentum-driven outflow.

#### 5.4. Final Picture

Our final picture of these sources is remarkably similar. Both sources show clear evidence of a low-velocity rotating disk comprised of warm molecular and low-IP ionized gases. Both sources show evidence of a decrement of warm molecular gas emission in the circum-nuclear region relative to warm ionized gas, evidence for radiative AGN feedback through the suppression of

star formation. Both sources show evidence of a highly ionized, high-velocity spatially stratified outflow in the unresolved nuclear emission. Finally, both sources show relatively low star formation rates, supporting the AGN-driven nature of the outflow.

The largest difference in the MIR observations of these sources comes in the detection of an extended high-velocity outflow in the warm ionized gas observations of F05189-2524, but not F11119+3257. The extent and velocity of this outflow decrease and increase, respectively, as the IP of the emission line increases. This seems to be consistent with the picture of a radiatively driven, spatially stratified outflow where higher velocities and IPs trace the region closest to the outflow axis and lower velocities trace the broader region around the edge. These extended emission maps show no evidence of a radial deceleration in the outflow.

Neither source shows any evidence for outflow in the warm molecular lines. Given the significance of the CO outflow detections in these sources relative to the disk strength, we cannot rule out the possibility that a weak resolved or unresolved outflow could be present in the warm molecular gas. In F05189-2524, we do see a turbulent, lower-density clump of molecular gas to the north of the quasar in the same direction as the warm ionized outflow. This is possibly indicative of the ionized outflow stirring up the molecular gas. The only other clear evidence of interaction between the two phases is the deficit of molecular gas relative to ionized gas in the nuclear region, likely caused by AGN-driven radiative feedback.

A schematic of the geometry of the MIR emission of both of these sources is displayed in Figure 13. The model shows the features discussed above: low-velocity rotational disks in both sources, unresolved high-velocity outflow, and resolved low-velocity molecular gas cloud, and high-velocity ionized gas outflow in F05189-2524.

## 6. CONCLUSION

We uniformly analyzed the MIR IFS data of two strikingly similar late-stage merger ULIRGs. Both sources have shown previous evidence for strong kpc-scale winds driven by a powerful AGN-driven UFO. The new *JWST* data provide the first high-resolution infrared view of the outflow and host galaxy in these merging galaxies. For both sources, we use `q3dfit` to separate the quasar light from the host galaxy and analyze emission markers of dust, molecular gas, and warm ionized gas to better understand the nature of these multiphase outflows. The main results of our analysis include:

1. In the unresolved nuclear emission, both sources show evidence of high-velocity ( $\sim 1500 \text{ km s}^{-1}$ ) ionized gas emission indicative of a nuclear-driven, spatially stratified outflow. We measure a mass outflow rate using the neon emission lines of  $10 - 14 \text{ } M_{\odot} \text{ yr}^{-1}$  in F11119+3257 and  $11 - 15 \text{ } M_{\odot} \text{ yr}^{-1}$  in F05189-2524. We see no evidence for any outflowing warm molecular gas.
2. Both sources show evidence of a deficit of molecular emission ( $\sim 100 \times$  weaker) relative to the warm ionized gas in the nuclear region ( $< 1 \text{ kpc}$ ). This deficit is roughly co-spatial with the rotating molecular and low-IP ionized gas disk and is evidence for radiative AGN feedback through suppression of molecular gas and star formation in the nuclear region of both galaxies.
3. In F05189-2524, we see evidence of a kpc-scale resolved high-velocity outflow in three neon emission lines [Ne III], [Ne V], and [Ne VI]. This emission increases in velocity and decreases in spatial extent as the IP of the line increases. The fastest emission is in the [Ne VI] line, which shows a flux-weighted median outflow  $|v_{50}| = 1060 \text{ km s}^{-1}$ . The furthest extent of the emission is in the [Ne III] line extending up to  $\sim 2 \text{ kpc}$  from the central quasar. [Ne III] represents  $\sim 80\%$  of the mass outflow rate, the dominant component. We estimate that  $\sim 90\%$  of this gas exceeds the escape velocity of the galaxy.
4. The addition of the warm ionized results does not drastically alter the energetic census of these sources, typically contributing  $\sim 0.1 - 5\%$  to the overall momentum outflow rate. In comparing the momentum outflow rate from the inner UFO-driven wind to the outer multiphase outflow, both of these sources are still broadly consistent with a momentum-conserving,  $\dot{P}_{\text{outer}}/\dot{P}_{\text{inner}} \sim 1$ , outflow.

K.Y.D., J.S., and S.V. acknowledge partial financial support by NASA for this research through STScI grants No. JWST-ERS-01335, JWST-GO-01865, JWST-GO-02547, JWST GO-03869, and JWST GO-05627. I.G.B. is supported by the Programa Atracción de Talento Investigador “César Nombela” via grant 2023-T1/TEC-29030 funded by the Community of Madrid. M.P.S. acknowledges support under grants RYC2021-033094-I, CNS2023-145506, and PID2023-146667NB-I00 funded by MCIN/AEI/10.13039/501100011033 and the European Union NextGenerationEU/PRTR.

## F05189-2524

## F11119+3257

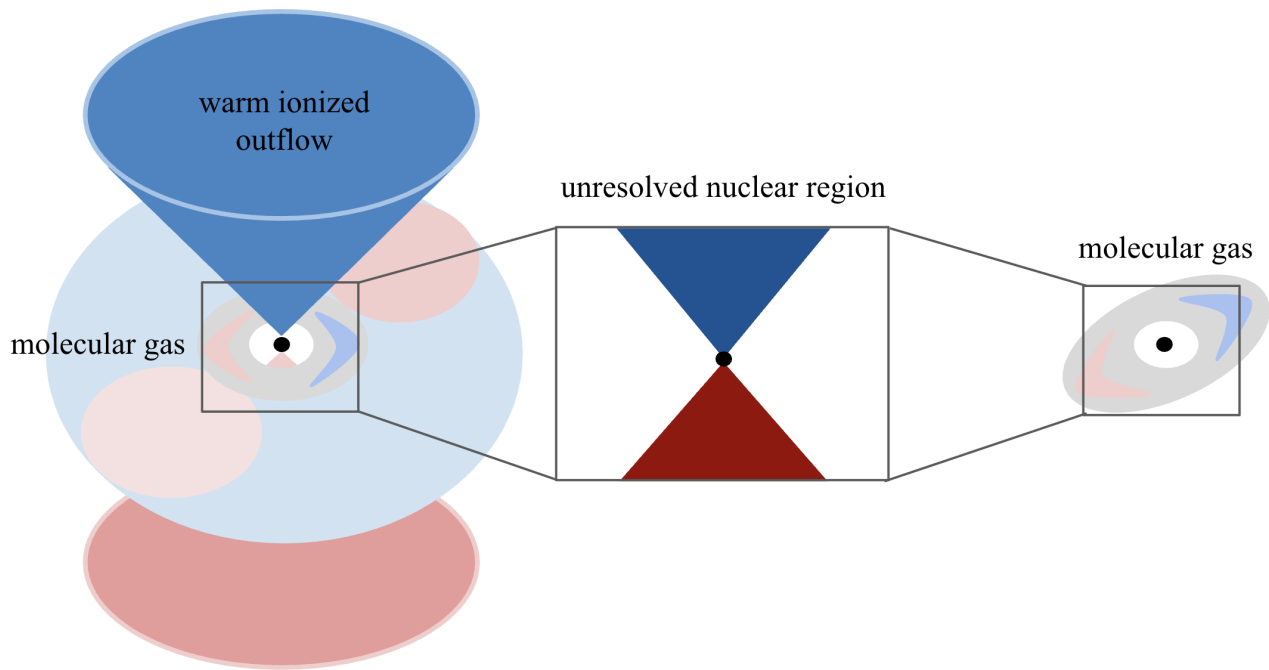


**Figure 13.** Schematic of the ionized outflows and surrounding disks in F05189-2524 (left) and F11119+3257 (right), derived by the *JWST* MIR observations. Both sources show a rotating molecular disk, with the disk for F05189-2524 oriented east to west and F11119+3257 oriented southeast to northwest, going from red to blue. The strength of the molecular disk weakens significantly directly around the quasar, illustrated by the white space. F05189-2524 also exhibits a low-velocity cloud of molecular gas around the quasar. In the unresolved nuclear regions, both sources show evidence for high-velocity warm ionized outflows, but we have no indication of the direction we represent this with the inset axis. F05189-2524 also shows a biconical, warm ionized outflow extending a few kpc from the quasar with velocities slightly lower than in the unresolved region.

Facilities: *JWST* MIRI MRS

Software: q3dfit (Rupke 2014, Rupke et al. 2021), Astropy (Astropy Collaboration et al. 2013, 2018), matplotlib (Hunter 2007), NumPy (Harris et al. 2020), SciPy (Virtanen et al. 2020)

## APPENDIX

## REFERENCES

Argyriou, I., Glasse, A., Law, D. R., et al. 2023, A&A, 675, A111, doi: [10.1051/0004-6361/202346489](https://doi.org/10.1051/0004-6361/202346489)

Astropy Collaboration, Robitaille, T. P., Tollerud, E. J., et al. 2013, A&A, 558, A33, doi: [10.1051/0004-6361/201322068](https://doi.org/10.1051/0004-6361/201322068)

Astropy Collaboration, Price-Whelan, A. M., Sipőcz, B. M., et al. 2018, AJ, 156, 123, doi: [10.3847/1538-3881/aabc4f](https://doi.org/10.3847/1538-3881/aabc4f)

Bushouse, H., Eisenhamer, J., Dencheva, N., et al. 2022, JWST Calibration Pipeline, 1.8.2, Zenodo, doi: [10.5281/zenodo.7325378](https://doi.org/10.5281/zenodo.7325378)

Bushouse, H., Eisenhamer, J., Dencheva, N., et al. 2024, JWST Calibration Pipeline, Zenodo

Ceci, M., Marconcini, C., Marconi, A., et al. 2025, arXiv e-prints, arXiv:2507.08077, doi: [10.48550/arXiv.2507.08077](https://doi.org/10.48550/arXiv.2507.08077)

Choi, E., Somerville, R. S., Ostriker, J. P., Naab, T., & Hirschmann, M. 2018, ApJ, 866, 91, doi: [10.3847/1538-4357/aae076](https://doi.org/10.3847/1538-4357/aae076)

Costa, T., Pakmor, R., & Springel, V. 2020, MNRAS, 497, 5229, doi: [10.1093/mnras/staa2321](https://doi.org/10.1093/mnras/staa2321)

Dan, K. Y., Seebeck, J., Veilleux, S., et al. 2025, *ApJ*, 979, 68, doi: [10.3847/1538-4357/ad9a50](https://doi.org/10.3847/1538-4357/ad9a50)

Davé, R., Anglés-Alcázar, D., Narayanan, D., et al. 2019, *MNRAS*, 486, 2827, doi: [10.1093/mnras/stz937](https://doi.org/10.1093/mnras/stz937)

Diamond-Stanic, A. M., & Rieke, G. H. 2012, *ApJ*, 746, 168, doi: [10.1088/0004-637X/746/2/168](https://doi.org/10.1088/0004-637X/746/2/168)

Draine, B. T., Li, A., Hensley, B. S., et al. 2021, *ApJ*, 917, 3, doi: [10.3847/1538-4357/abff51](https://doi.org/10.3847/1538-4357/abff51)

Dubois, Y., Peirani, S., Pichon, C., et al. 2016, *MNRAS*, 463, 3948, doi: [10.1093/mnras/stw2265](https://doi.org/10.1093/mnras/stw2265)

Farrah, D., Bernard-Salas, J., Spoon, H. W. W., et al. 2007, *ApJ*, 667, 149, doi: [10.1086/520834](https://doi.org/10.1086/520834)

Fiore, F., Feruglio, C., Shankar, F., et al. 2017, *A&A*, 601, A143, doi: [10.1051/0004-6361/201629478](https://doi.org/10.1051/0004-6361/201629478)

Fluetsch, A., Maiolino, R., Carniani, S., et al. 2019, *MNRAS*, 483, 4586, doi: [10.1093/mnras/sty3449](https://doi.org/10.1093/mnras/sty3449)

Gallo, L. C., Miller, J. M., & Costantini, E. 2023, arXiv e-prints, arXiv:2302.10930, doi: [10.48550/arXiv.2302.10930](https://doi.org/10.48550/arXiv.2302.10930)

García-Bernete, I., Rigopoulou, D., Alonso-Herrero, A., et al. 2022a, *MNRAS*, 509, 4256, doi: [10.1093/mnras/stab3127](https://doi.org/10.1093/mnras/stab3127)

—. 2022b, *A&A*, 666, L5, doi: [10.1051/0004-6361/202244806](https://doi.org/10.1051/0004-6361/202244806)

Gaspari, M., Tombesi, F., & Cappi, M. 2020, *Nature Astronomy*, 4, 10, doi: [10.1038/s41550-019-0970-1](https://doi.org/10.1038/s41550-019-0970-1)

González-Alfonso, E., Fischer, J., Spoon, H. W. W., et al. 2017, *ApJ*, 836, 11, doi: [10.3847/1538-4357/836/1/11](https://doi.org/10.3847/1538-4357/836/1/11)

Groves, B., Dopita, M., & Sutherland, R. 2006, *A&A*, 458, 405, doi: [10.1051/0004-6361:20065097](https://doi.org/10.1051/0004-6361:20065097)

Habart, E., Walmsley, M., Verstraete, L., et al. 2005, *SSRv*, 119, 71, doi: [10.1007/s11214-005-8062-1](https://doi.org/10.1007/s11214-005-8062-1)

Harris, C. R., Millman, K. J., van der Walt, S. J., et al. 2020, *Nature*, 585, 357, doi: [10.1038/s41586-020-2649-2](https://doi.org/10.1038/s41586-020-2649-2)

Hickox, R. C., & Alexander, D. M. 2018, *ARA&A*, 56, 625, doi: [10.1146/annurev-astro-081817-051803](https://doi.org/10.1146/annurev-astro-081817-051803)

Hopkins, P. F., Hernquist, L., Cox, T. J., & Kereš, D. 2008, *ApJS*, 175, 356, doi: [10.1086/524362](https://doi.org/10.1086/524362)

Hopkins, P. F., Torrey, P., Faucher-Giguère, C.-A., Quataert, E., & Murray, N. 2016, *MNRAS*, 458, 816, doi: [10.1093/mnras/stw289](https://doi.org/10.1093/mnras/stw289)

Houck, J. R., Schneider, D. P., Danielson, G. E., et al. 1985, *ApJL*, 290, L5, doi: [10.1086/184431](https://doi.org/10.1086/184431)

Hunter, J. D. 2007, *Computing in Science & Engineering*, 9, 90, doi: [10.1109/MCSE.2007.55](https://doi.org/10.1109/MCSE.2007.55)

Jones, L. H., Hernandez, S., Smith, L. J., et al. 2024, arXiv e-prints, arXiv:2410.09020, doi: [10.48550/arXiv.2410.09020](https://doi.org/10.48550/arXiv.2410.09020)

King, A., & Pounds, K. 2015, *ARA&A*, 53, 115, doi: [10.1146/annurev-astro-082214-122316](https://doi.org/10.1146/annurev-astro-082214-122316)

Laha, S., Reynolds, C. S., Reeves, J., et al. 2021, *Nature Astronomy*, 5, 13, doi: [10.1038/s41550-020-01255-2](https://doi.org/10.1038/s41550-020-01255-2)

Lamperti, I., Pereira-Santaella, M., Perna, M., et al. 2022, *A&A*, 668, A45, doi: [10.1051/0004-6361/202244054](https://doi.org/10.1051/0004-6361/202244054)

Lanzuisi, G., Matzeu, G., Baldini, P., et al. 2024, *A&A*, 689, A247, doi: [10.1051/0004-6361/202449194](https://doi.org/10.1051/0004-6361/202449194)

Law, D. R., E. Morrison, J., Argyriou, I., et al. 2023, *AJ*, 166, 45, doi: [10.3847/1538-3881/acddd](https://doi.org/10.3847/1538-3881/acddd)

Li, A. 2020, *Nature Astronomy*, 4, 339, doi: [10.1038/s41550-020-1051-1](https://doi.org/10.1038/s41550-020-1051-1)

Liu, W., Veilleux, S., Canalizo, G., et al. 2020, *ApJ*, 905, 166, doi: [10.3847/1538-4357/abc269](https://doi.org/10.3847/1538-4357/abc269)

Liu, W., Veilleux, S., Rupke, D. S. N., et al. 2022, *ApJ*, 934, 160, doi: [10.3847/1538-4357/ac7a46](https://doi.org/10.3847/1538-4357/ac7a46)

Liu, W., Veilleux, S., Iwasawa, K., et al. 2019, *ApJ*, 872, 39, doi: [10.3847/1538-4357/aafdfc](https://doi.org/10.3847/1538-4357/aafdfc)

Luridiana, V., Morisset, C., & Shaw, R. A. 2015, *A&A*, 573, A42, doi: [10.1051/0004-6361/201323152](https://doi.org/10.1051/0004-6361/201323152)

Lutz, D., Sturm, E., Tacconi, L. J., et al. 2008, *ApJ*, 684, 853, doi: [10.1086/590367](https://doi.org/10.1086/590367)

Lutz, D., Sturm, E., Janssen, A., et al. 2020, *A&A*, 633, A134, doi: [10.1051/0004-6361/201936803](https://doi.org/10.1051/0004-6361/201936803)

Maragkoudakis, A., Peeters, E., & Ricca, A. 2020, *MNRAS*, 494, 642, doi: [10.1093/mnras/staa681](https://doi.org/10.1093/mnras/staa681)

Marasco, A., Cresci, G., Nardini, E., et al. 2020, *A&A*, 644, A15, doi: [10.1051/0004-6361/202038889](https://doi.org/10.1051/0004-6361/202038889)

Matzeu, G. A., Brusa, M., Lanzuisi, G., et al. 2023, *A&A*, 670, A182, doi: [10.1051/0004-6361/202245036](https://doi.org/10.1051/0004-6361/202245036)

Nardini, E., & Zubovas, K. 2018, *MNRAS*, 478, 2274, doi: [10.1093/mnras/sty1144](https://doi.org/10.1093/mnras/sty1144)

Nicholls, D. C., Sutherland, R. S., Dopita, M. A., Kewley, L. J., & Groves, B. A. 2017, *MNRAS*, 466, 4403, doi: [10.1093/mnras/stw3235](https://doi.org/10.1093/mnras/stw3235)

Noda, H., Yamada, S., Ogawa, S., et al. 2025, *ApJL*, 993, L53, doi: [10.3847/2041-8213/ae14e8](https://doi.org/10.3847/2041-8213/ae14e8)

Pan, X., Zhou, H., Liu, W., et al. 2019, *ApJ*, 883, 173, doi: [10.3847/1538-4357/ab40b5](https://doi.org/10.3847/1538-4357/ab40b5)

Peeters, E., Spoon, H. W. W., & Tielens, A. G. G. M. 2004, *ApJ*, 613, 986, doi: [10.1086/423237](https://doi.org/10.1086/423237)

Pereira-Santaella, M., Spinoglio, L., van der Werf, P. P., & Piqueras López, J. 2014, *A&A*, 566, A49, doi: [10.1051/0004-6361/201423430](https://doi.org/10.1051/0004-6361/201423430)

Pereira-Santaella, M., Álvarez-Márquez, J., García-Bernete, I., et al. 2022, *A&A*, 665, L11, doi: [10.1051/0004-6361/202244725](https://doi.org/10.1051/0004-6361/202244725)

Pontzen, A., Tremmel, M., Roth, N., et al. 2017, *MNRAS*, 465, 547, doi: [10.1093/mnras/stw2627](https://doi.org/10.1093/mnras/stw2627)

Pope, A., Chary, R.-R., Alexander, D. M., et al. 2008, *ApJ*, 675, 1171, doi: [10.1086/527030](https://doi.org/10.1086/527030)

Rigopoulou, D., Kunze, D., Lutz, D., Genzel, R., & Moorwood, A. F. M. 2002, A&A, 389, 374, doi: [10.1051/0004-6361:20020607](https://doi.org/10.1051/0004-6361:20020607)

Rigopoulou, D., Barale, M., Clary, D. C., et al. 2021, MNRAS, 504, 5287, doi: [10.1093/mnras/stab959](https://doi.org/10.1093/mnras/stab959)

Rigopoulou, D., Donnan, F. R., García-Bernete, I., et al. 2024, MNRAS, 532, 1598, doi: [10.1093/mnras/stae1535](https://doi.org/10.1093/mnras/stae1535)

Robitaille, T., Ginsburg, A., Mumford, S., et al. 2024, astropy/reproject: v0.13.1, v0.13.1, Zenodo, doi: [10.5281/zenodo.10931886](https://doi.org/10.5281/zenodo.10931886)

Roueff, E., Abgrall, H., Czachorowski, P., et al. 2019, A&A, 630, A58, doi: [10.1051/0004-6361/201936249](https://doi.org/10.1051/0004-6361/201936249)

Rupke, D., Wylezalek, D., Zakamska, N., et al. 2023a, q3dfit: PSF decomposition and spectral analysis for JWST-IFU spectroscopy, Astrophysics Source Code Library, record ascl:2310.004

Rupke, D. S., Veilleux, S., & Sanders, D. B. 2005, ApJ, 632, 751, doi: [10.1086/444451](https://doi.org/10.1086/444451)

Rupke, D. S. N. 2014, IFSFIT: Spectral Fitting for Integral Field Spectrographs, Astrophysics Source Code Library, record ascl:1409.005. <http://ascl.net/1409.005>

Rupke, D. S. N., Göltekin, K., & Veilleux, S. 2017, ApJ, 850, 40, doi: [10.3847/1538-4357/aa94d1](https://doi.org/10.3847/1538-4357/aa94d1)

Rupke, D. S. N., Schweitzer, M., Viola, V., et al. 2021, QUESTFIT: Fitter for mid-infrared galaxy spectra, Astrophysics Source Code Library, record ascl:2112.002. <http://ascl.net/2112.002>

Rupke, D. S. N., & Veilleux, S. 2013, ApJ, 768, 75, doi: [10.1088/0004-637X/768/1/75](https://doi.org/10.1088/0004-637X/768/1/75)

Rupke, D. S. N., Wylezalek, D., Zakamska, N. L., et al. 2023b, ApJL, 953, L26, doi: [10.3847/2041-8213/aced85](https://doi.org/10.3847/2041-8213/aced85)

Sanders, D. B., Soifer, B. T., Elias, J. H., Neugebauer, G., & Matthews, K. 1988, ApJL, 328, L35, doi: [10.1086/185155](https://doi.org/10.1086/185155)

Schneider, E. E., & Mao, S. A. 2024, ApJ, 966, 37, doi: [10.3847/1538-4357/ad2e8a](https://doi.org/10.3847/1538-4357/ad2e8a)

Schweitzer, M., Lutz, D., Sturm, E., et al. 2006, ApJ, 649, 79, doi: [10.1086/506510](https://doi.org/10.1086/506510)

Schweitzer, M., Groves, B., Netzer, H., et al. 2008, ApJ, 679, 101, doi: [10.1086/587097](https://doi.org/10.1086/587097)

Seebeck, J., Veilleux, S., Liu, W., et al. 2024, ApJ, 976, 240, doi: [10.3847/1538-4357/ad815e](https://doi.org/10.3847/1538-4357/ad815e)

Shipley, H. V., Papovich, C., Rieke, G. H., Brown, M. J. I., & Moustakas, J. 2016, ApJ, 818, 60, doi: [10.3847/0004-637X/818/1/60](https://doi.org/10.3847/0004-637X/818/1/60)

Siebenmorgen, R., Krügel, E., & Spoon, H. W. W. 2004, A&A, 414, 123, doi: [10.1051/0004-6361:20031633](https://doi.org/10.1051/0004-6361:20031633)

Smith, J. D. T., Draine, B. T., Dale, D. A., et al. 2007, ApJ, 656, 770, doi: [10.1086/510549](https://doi.org/10.1086/510549)

Smith, R. N., Tombesi, F., Veilleux, S., Lohfink, A. M., & Luminari, A. 2019, ApJ, 887, 69, doi: [10.3847/1538-4357/ab4ef8](https://doi.org/10.3847/1538-4357/ab4ef8)

Spoon, H. W. W., & Holt, J. 2009, ApJL, 702, L42, doi: [10.1088/0004-637X/702/1/L42](https://doi.org/10.1088/0004-637X/702/1/L42)

Togi, A., & Smith, J. D. T. 2016, ApJ, 830, 18, doi: [10.3847/0004-637X/830/1/18](https://doi.org/10.3847/0004-637X/830/1/18)

Tombesi, F., Cappi, M., Reeves, J. N., et al. 2010, A&A, 521, A57, doi: [10.1051/0004-6361/200913440](https://doi.org/10.1051/0004-6361/200913440)

Tombesi, F., Meléndez, M., Veilleux, S., et al. 2015, Nature, 519, 436, doi: [10.1038/nature14261](https://doi.org/10.1038/nature14261)

Tombesi, F., Tazaki, F., Mushotzky, R. F., et al. 2014, MNRAS, 443, 2154, doi: [10.1093/mnras/stu1297](https://doi.org/10.1093/mnras/stu1297)

Tombesi, F., Veilleux, S., Meléndez, M., et al. 2017, ApJ, 850, 151, doi: [10.3847/1538-4357/aa9579](https://doi.org/10.3847/1538-4357/aa9579)

Treyer, M., Schiminovich, D., Johnson, B. D., et al. 2010, ApJ, 719, 1191, doi: [10.1088/0004-637X/719/2/1191](https://doi.org/10.1088/0004-637X/719/2/1191)

Tumlinson, J., Peeples, M. S., & Werk, J. K. 2017, ARA&A, 55, 389, doi: [10.1146/annurev-astro-091916-055240](https://doi.org/10.1146/annurev-astro-091916-055240)

Vayner, A., Zakamska, N. L., Ishikawa, Y., et al. 2023, ApJ, 955, 92, doi: [10.3847/1538-4357/ace784](https://doi.org/10.3847/1538-4357/ace784)

Veilleux, S. 1991a, ApJ, 369, 331, doi: [10.1086/169765](https://doi.org/10.1086/169765)

—. 1991b, ApJS, 75, 357, doi: [10.1086/191534](https://doi.org/10.1086/191534)

—. 1991c, ApJS, 75, 383, doi: [10.1086/191535](https://doi.org/10.1086/191535)

Veilleux, S., Bolatto, A., Tombesi, F., et al. 2017, ApJ, 843, 18, doi: [10.3847/1538-4357/aa767d](https://doi.org/10.3847/1538-4357/aa767d)

Veilleux, S., Cecil, G., & Bland-Hawthorn, J. 2005, ARA&A, 43, 769, doi: [10.1146/annurev.astro.43.072103.150610](https://doi.org/10.1146/annurev.astro.43.072103.150610)

Veilleux, S., Maiolino, R., Bolatto, A. D., & Aalto, S. 2020, A&A Rv, 28, 2, doi: [10.1007/s00159-019-0121-9](https://doi.org/10.1007/s00159-019-0121-9)

Veilleux, S., Sanders, D. B., & Kim, D. C. 1999, ApJ, 522, 139, doi: [10.1086/307635](https://doi.org/10.1086/307635)

Veilleux, S., Teng, S. H., Rupke, D. S. N., Maiolino, R., & Sturm, E. 2014, ApJ, 790, 116, doi: [10.1088/0004-637X/790/2/116](https://doi.org/10.1088/0004-637X/790/2/116)

Veilleux, S., Kim, D. C., Peng, C. Y., et al. 2006, ApJ, 643, 707, doi: [10.1086/503188](https://doi.org/10.1086/503188)

Veilleux, S., Rupke, D. S. N., Kim, D.-C., et al. 2009a, ApJS, 182, 628, doi: [10.1088/0067-0049/182/2/628](https://doi.org/10.1088/0067-0049/182/2/628)

Veilleux, S., Kim, D. C., Rupke, D. S. N., et al. 2009b, ApJ, 701, 587, doi: [10.1088/0004-637X/701/1/587](https://doi.org/10.1088/0004-637X/701/1/587)

Veilleux, S., Meléndez, M., Sturm, E., et al. 2013, ApJ, 776, 27, doi: [10.1088/0004-637X/776/1/27](https://doi.org/10.1088/0004-637X/776/1/27)

Veilleux, S., Liu, W., Vayner, A., et al. 2023, ApJ, 953, 56, doi: [10.3847/1538-4357/ace10f](https://doi.org/10.3847/1538-4357/ace10f)

Virtanen, P., Gommers, R., Oliphant, T. E., et al. 2020, Nature Methods, 17, 261, doi: [10.1038/s41592-019-0686-2](https://doi.org/10.1038/s41592-019-0686-2)

Voit, G. M. 1992, MNRAS, 258, 841,  
doi: [10.1093/mnras/258.4.841](https://doi.org/10.1093/mnras/258.4.841)

Volonteri, M., Dubois, Y., Pichon, C., & Devriendt, J.  
2016, MNRAS, 460, 2979, doi: [10.1093/mnras/stw1123](https://doi.org/10.1093/mnras/stw1123)

Wagner, A. Y., Umemura, M., & Bicknell, G. V. 2013,  
ApJL, 763, L18, doi: [10.1088/2041-8205/763/1/L18](https://doi.org/10.1088/2041-8205/763/1/L18)

Wright, G. S., Rieke, G. H., Glasse, A., et al. 2023, PASP,  
135, 048003, doi: [10.1088/1538-3873/acbe66](https://doi.org/10.1088/1538-3873/acbe66)

Xrism Collaboration, Audard, M., Awaki, H., et al. 2025,  
Nature, 641, 1132, doi: [10.1038/s41586-025-08968-2](https://doi.org/10.1038/s41586-025-08968-2)

Youngblood, A., France, K., Ginsburg, A., Hoadley, K., &  
Bally, J. 2018, ApJ, 857, 7,  
doi: [10.3847/1538-4357/aab4f4](https://doi.org/10.3847/1538-4357/aab4f4)

Zakamska, N. L., & Greene, J. E. 2014, MNRAS, 442, 784,  
doi: [10.1093/mnras/stu842](https://doi.org/10.1093/mnras/stu842)

Zakamska, N. L., Hamann, F., Pâris, I., et al. 2016,  
MNRAS, 459, 3144, doi: [10.1093/mnras/stw718](https://doi.org/10.1093/mnras/stw718)

Zhang, L., Packham, C., Hicks, E. K. S., et al. 2024, ApJ,  
974, 195, doi: [10.3847/1538-4357/ad6a4b](https://doi.org/10.3847/1538-4357/ad6a4b)

Zubovas, K., & King, A. 2012, ApJL, 745, L34,  
doi: [10.1088/2041-8205/745/2/L34](https://doi.org/10.1088/2041-8205/745/2/L34)